# Seismic evidence for a two-stage origin of the October 2026 Budhi Gandaki landslide in the Nepal Himalaya

Christopher M. Calvelage[1,*], Shuye Huang[2], Chan-Mao Chen[3], Binhao Wang[4], Beth Pratt-Sitaula[1] and J. Mitchell McLaughlin[5]

[1] EarthScope Consortium, Washington, D.C., USA
[2] Earthquake Research Institute, The University of Tokyo, Tokyo, Japan
[3] Department of Earth Sciences, University of Southern California, Los Angeles, CA, USA
[4] Scripps Institution of Oceanography, University of California San Diego, La Jolla, CA, USA
[5] New Mexico Institute of Mining and Technology, Socorro, New Mexico, USA

[*] Corresponding author, chris.calvelage@earthscope.org

ORCID: C. M. Calvelage 0009-0005-9807-4255, S. Huang 0000-0002-0907-8694, C.-M. Chen 0009-0002-0897-3459, B. Wang 0000-0001-6934-1522, B. Pratt-Sitaula 0000-0001-7499-7286, J. M. McLaughlin 0009-0002-1077-0140

**This manuscript is a non-peer-reviewed preprint submitted to EarthArXiv.**
It has been submitted to *Seismica* for publication as a Fast Report and has not yet been peer reviewed. Subsequent versions of this manuscript may have slightly different content. If accepted, the final version will be available via the "Peer-reviewed Publication DOI" link on the right-hand side of this webpage. Please feel free to contact the corresponding author; we welcome feedback.

This file contains the manuscript followed by its Supplementary Material.

The analysis code and derivative products are archived on Zenodo at `https://doi.org/10.5281/zenodo.24143591`.

Version of 11 November 2026.

Non-peer reviewed **Fast Report** submitted to SEISMICA

# Seismic evidence for a two-stage origin of the October 2026 Budhi Gandaki landslide in the Nepal Himalaya

**Christopher M. Calvelage** * [1], **Shuye Huang** [2], **Chan-Mao Chen** [3], **Binhao Wang** [4], **Beth Pratt-Sitaula** [1], **J. Mitchell McLaughlin** [5]

[1]EarthScope Consortium, Washington, D.C., USA, [2]Earthquake Research Institute, The University of Tokyo, Tokyo, Japan, [3]Department of Earth Sciences, University of Southern California, Los Angeles, CA, USA, [4]Scripps Institution of Oceanography, University of California San Diego, La Jolla, CA, USA, [5]New Mexico Institute of Mining and Technology, Socorro, New Mexico, USA

Author contributions: *Conceptualization, Software, Visualization, Writing - Original draft*: Christopher M. Calvelage. *Methodology, Formal Analysis, Investigation, Data Curation, Writing - Review & Editing*: all authors.

**Abstract** On 10 October 2026 a rock avalanche left the south face of the Chamar massif, Nepal, ran 8.7 km down the Ungilung and dammed the Shyar River above the Budhi Gandaki. Single-force inversions of one regional and 28 teleseismic records resolve four force pulses 23–26 s apart, alternating westward and eastward. Flow simulations released from the face favor two stages of failure, a smaller one at the onset of the high-frequency signal and the main body 40–60 s later, together 6–21 $Mm^3$, reaching the Shyar in three minutes.

**Non-technical summary** A section of the Chamar massif above the Budhi Gandaki valley of Nepal collapsed early on 11 October 2026, local time, and caused a flood down the valley. When a mountainside collapses, the force it exerts on the ground is recorded as a seismic signal that can propagate for hundreds to thousands of kilometers. The seismic signal, compared with simulations of the flowing rock, indicates that the rock left the face in two stages, a small landslide first and a larger landslide 40 to 60 s later, 6 to 21 million cubic meters in all, which reached the Shyar River within three minutes.

*Corresponding author: chris.calvelage@earthscope.org

# 1 Introduction

Large rock avalanches in high mountain environments can initiate cascading hazards that threaten communities and infrastructure far downstream of their source slopes (Hancox et al., 2005; Shugar et al., 2021; Adhikari et al., 2026). Understanding these events requires resolving the sequence of processes that links the slope failure to the downstream impacts. Seismic records constrain the timing, the mass and the kinetics of a failure, from which its sequence and the forces it exerted on the Earth can be reconstructed.

A large flood struck central Nepal on 11 October 2026 in the Budhi Gandaki River, Gorkha district. The flood originated from a rock avalanche on the south face of the Chamar massif at 22:37:40 UTC on 10 October 2026, 04:22 Nepal time on 11 October (Fig. 1). The avalanche descended the Ungilung Khola, and its debris dammed the Shyar Khola in the Tsum valley. The dam breached repeatedly. The first surge reached Salleri about ten minutes after the landslide and the largest, 20–25 m high, about two hours after it (National Disaster Risk Reduction and Management Authority (NDRRMA), 2026). The flood likely killed five people, destroyed houses and bridges along 50 km of river, and damaged a hydropower project (National Disaster Risk Reduction and Management Authority (NDRRMA), 2026; Petley, 2026).

The record of the nearest station begins with a minute of weak high-frequency energy before the main signal (Fig. 2A), which raises the question whether the avalanche began as a single release or in several stages. Here we invert the records of one regional and 28 teleseismic stations for the force history, using teleseismic Green's functions corrected for three-dimensional structure. We then compare the observed records and the inverted forces with flow simulations released from the mapped source face, to test alternative release histories and to constrain the timing, motion and mass of the avalanche.

# 2 Event, data and methods

## 2.1 Source and data

The source is interpreted to be the south face of the Chamar massif at 28.54°N, 84.94°E, below its 7050-m south summit and at the head of the Ungilung Khola (Fig. 1A, D). A public PlanetScope comparison of 1 and 14 October (Shugar, 2026), georeferenced to within 7 m (Supplement S2), shows snow stripped from 0.31 $km^2$ of the face between 5800 and 6700 m, which is dark on cloud-

free Sentinel-2 scenes of 21–26 October (Fig. S3C), and 0.31 km$^2$ of dark debris on the glacier at 4700–5470 m (Fig. S3D). On the Copernicus GLO-30 elevation model (European Space Agency and Airbus, 2022), within 600 m of the release center, the face is 0.93 km$^2$ steeper than 35° between 5500 and 6700 m, mean slope 52°. The path falls 1300 m down the face to its base at 5400 m, runs southwest to a bend at 3800 m and south to the Shyar at 2028 m, 5 km above the Budhi Gandaki (Fig. 1C, E).

The regional record is from NK.KKN at Kakani (88 km, azimuth 158°), the only open broadband station within 500 km with a record of the event (Fig. 1A). We define the time origin as 22:37:40 UTC, the 1–10 Hz onset at KKN, and give the times of the failure stages, the force pulses and the flow in seconds from it. Twenty-eight stations between 11° and 36° recorded the 35–100 s Rayleigh waves with a signal-to-noise ratio above 3 (Fig. 1B); 19 of them lie in the 270–360° azimuth sector, and 14, all closer than 25°, also give usable horizontal records. Nine near-field stations within 2° of the source, at 158–258° in azimuth (Fig. 1A), give the 1–2 Hz data of Section 3.3. For the near-field apparent radiation pattern (Huang et al., 2026) we take the root-mean-square vertical amplitude at 1–2 Hz in 30-s windows every 15 s, moved to source time with the S-wave travel time and normalized by the station's mean over 30–450 s and by the network mean, and fit the nine values with an isotropic and a two-lobed term, $A_0 + A_2\,|\cos(\phi - \theta)|$, whose axis $\theta$ we compare with the normal to the simulated front (Section 3.3).

## 2.2 Single-force inversions

Large landslides exert forces on the Earth equal and opposite to the rate of change of their momentum, and the long-period waves they radiate can be inverted for these forces (Kanamori and Given, 1982; Fukao, 1995; Ekström and Stark, 2013). These forces scale empirically with the mass (Ekström and Stark, 2013; Chao et al., 2016). The force history records the accelerations and impacts of the center of mass (Allstadt, 2013; Hibert et al., 2014; Moretti et al., 2020). With sufficient station coverage, these records can constrain the direction of motion and help distinguish whether a slope failure occurred in a single stage or in several.

The inversions use Syngine single-force Green's functions (Nissen-Meyer et al., 2014; Krischer et al., 2017) for ak135f (Kennett et al., 1995) and PREM (Dziewonski and Anderson, 1981), the force on a 1-s grid, a norm plus second-difference regularization at the L-curve corner, and station shifts by coordinate descent (Eqs. S1–S2). KKN is inverted on its three components at 20–80 s. The teleseismic inversions use four data sets, (1) the 28 verticals at 35–100 s, (2) the 28 horizontals (Love

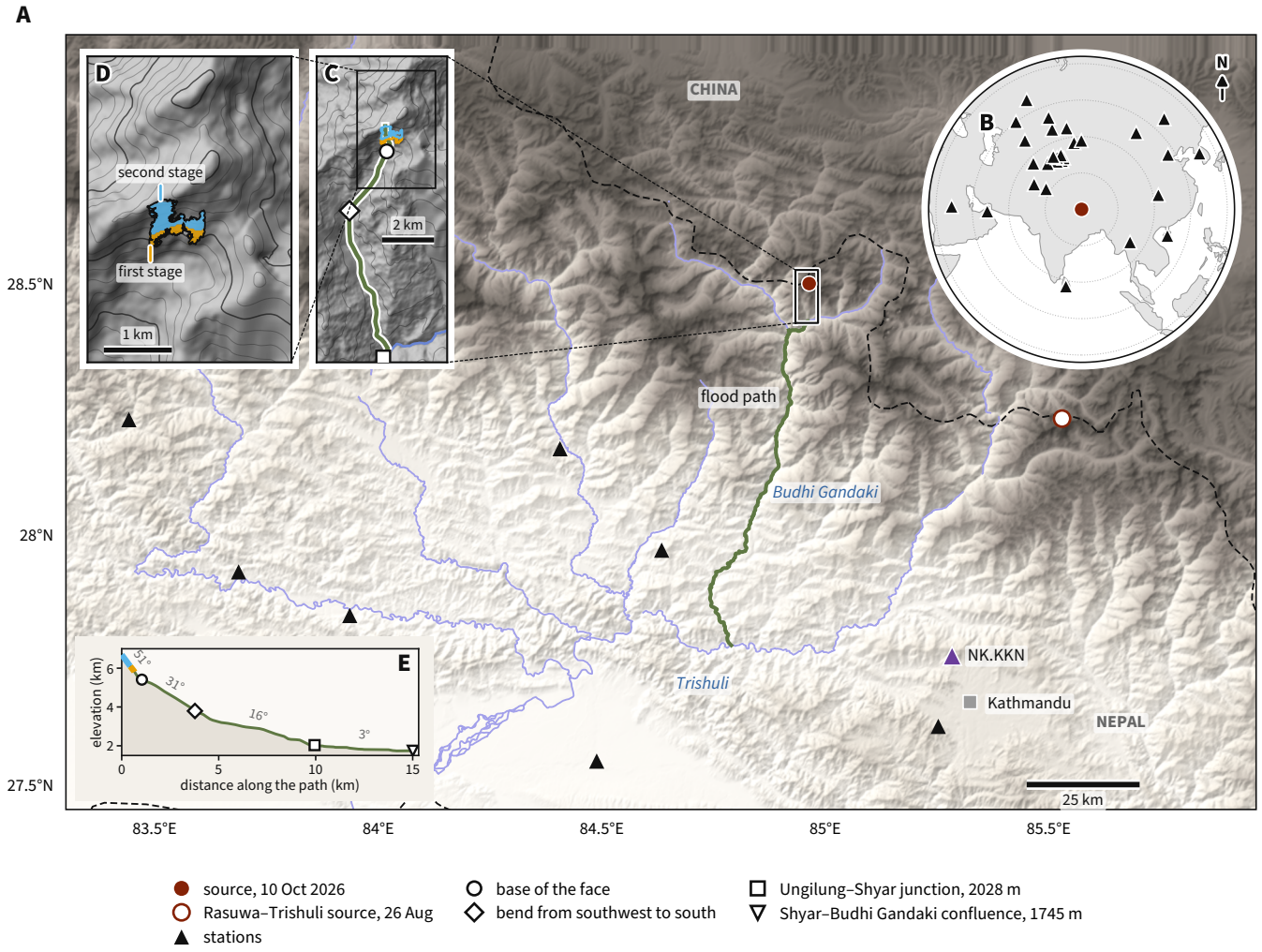



**Figure 1** Setting, data and model set-up. (A) The source, NK.KKN, the near-field stations of the 1–2 Hz fit of Fig. 4K and the 26 August Rasuwa–Trishuli source on GLO-90 relief in UTM 45N, with the flood path down the Shyar and Budhi Gandaki, other rivers in pale blue, borders dashed, the extent of C as a rectangle and a 25-km bar; the ninth station of the fit, AM.RCCCC, lies 211 km west of the source, beyond the frame. B to E are insets of A. (B) The 28 teleseismic stations with verticals at 35–100 s on an azimuthal equidistant map about the source, with rings every 10°; 14 of them also give the 35–150 s verticals and 14 the horizontals (Section 2.1). (C) The flow-model domain reached by the simulations, with the path along the fall line and the Ungilung to the Shyar junction, the release zones, the Shyar and the extent of D. (D) The scar on the GLO-30 hillshade (200-m contours, heavier every 1000 m), the outline of the face stripped of snow between 1 and 14 October in the public PlanetScope comparison (black; Fig. S3) and the release zones of the two stages of the best simulation, below and above 6100 m and 50 s apart (Fig. 4). (E) Elevation against horizontal distance along the path at true scale, with the release zones, the landmarks of C and the mean slope of each segment, continued down the Shyar to its confluence with the Budhi Gandaki (triangle).

waves) and (3) both together (56 traces) in the same band, and (4) 14 of the verticals at 35–150 s. The KKN band reaches 20 s because its short path needs no corrections, and the teleseismic bands begin at 35 s, the shortest period of the REM3D maps, and end where the signal-to-noise ratio of the Rayleigh waves falls. The teleseismic Green's functions are corrected for three-dimensional structure with the REM3D fundamental-mode phase-delay maps (Moulik et al., 2021), which are sampled along each path and applied as a dispersive phase factor per period, Rayleigh maps for the vertical and radial components and Love maps for the transverse component (Supplement S1). On the Tibetan paths the REM3D delays reach +81 s at 35 s. The delays that remain, measured on 14 regional earthquakes, are removed station by station below 60 s and tapered out by 75 s, which halves the remaining phase error at 35–45 s (Supplement S1) and brings the largest 35-s delay to 93 s for PREM and 115 s for ak135f. The corrected inversions explain 0.35–0.56 of the variance of the four sets, 0.03–0.18 more than with one-dimensional functions.

### 2.3 Flow model

The flow model is r.avaflow 3 (Mergili et al., 2017; Mergili and Pudasaini, 2023), one-phase and Voellmy-type, patched to log the first moments of the mass, from which the force on the Earth follows as $-M\,\mathrm{d}^2\mathbf{r}_{cm}/\mathrm{d}t^2$, the mass $M$ times the acceleration of its center of mass $\mathbf{r}_{cm}$, with the sign reversed (Ekström and Stark, 2013; Moretti et al., 2015), on GLO-30 at 30 m. The release zone is the steep face of Section 2.1 (0.93 km$^2$), with a paraboloid thickness scaled to the volume. A two-stage release holds its second zone as terrain until a time $t_2$. The flow is slowed by Coulomb friction at its base, not by internal friction of the material, with a basal friction angle $\delta$ within 2 km of the release and a smaller angle $\delta_{\mathrm{far}}$ farther along the path, and by a Voellmy drag that grows with the square of the speed. The drag coefficient $\xi$, in m s$^{-2}$, is larger when the drag is weaker, so it sets the speed the flow can reach. The release time of a simulation, the instant at which its mass is set in motion, is not known in advance. We therefore shift its synthetics over a range of candidate release times and keep the time at which they fit the data best. At KKN, on 20–80 s synthetics, the fit is measured by the variance reduction at the best amplitude, by the correlation with the inversion's synthetics and by the correlation of the simulated with the inverted force per component. On the four teleseismic sets, with corrected Green's functions, it is measured by the correlation and the amplitude factor of the simulation's synthetics against the inversion's (Eq. S5). The amplitude factor times the simulated mass gives the mass implied by the data. The design comprises 28 simulations of 480 s, single-stage releases of 10–30 Mm$^3$ with $\log_{10}\xi$ of 3.0, 3.5 and

4.0, $\delta$ of 10–16° and $\delta_{\mathrm{far}}$ of 2–5°, two-stage releases of the lower and upper face in either order (8 + 16 and 5 + 15 $\mathrm{Mm}^3$, the second stage at 35–80 s), and three releases from the mapped outline.

# 3 Results and discussion

## 3.1 The inverted force

All five inversions show the same east–west alternation of the horizontal force (Fig. 2D). The force points west at 60–62 s after the 1–10 Hz onset, east at 85 s, west at 108–109 s, east at 134 s and west at 150–180 s, and the sequence is recovered by each data set; the five solutions agree on the pulse times within 10 s and azimuths within 40° (Fig. 4I). The KKN inversion explains 0.90 of the variance of its record (Fig. 2B). The corrected 35–100 s vertical inversion explains 0.52 of the variance of its 28 records, and −0.26 to 0.89 at individual stations (Fig. 2C). The peak force of the five solutions is 1.5–2.6 $\times 10^{11}$ N (Fig. S2).

The vertical component determines the sense of each pulse. A mass that accelerates exerts an upward and backward force on the Earth, and one that decelerates or impacts a downward and forward force, so the vertical sign paired with the east–west sign shows whether the mass accelerated westward or eastward. With one-dimensional Green's functions the data sets disagree on the sense of the pulses, and the teleseismic pulses scatter by up to 17 s about those of KKN (Fig. S1A). With the corrected functions, both Earth models and both bands reproduce the four KKN pulses in absolute time to within 4 s (Fig. 2D), and their vertical force shows the same pattern as KKN, downward during the westward pulses and upward during the eastward ones (Fig. 2E). The KKN force correlates at 0.50–0.69 with the corrected teleseismic synthetics at 35–100 s, compared with 0.09–0.26 before the correction. The three-dimensional corrections are therefore needed to recover the timing and sense of the force. The inverted force indicates a mass moving westward, which decelerated at 60–62 and 108–109 s and accelerated at 85 and 134 s.

The vertical amplitudes of the solutions differ, the KKN vertical being 1.5–1.8 times the teleseismic ones with ak135f functions and 1.1–1.4 times with PREM (Fig. 2E). The north force, 0.2–0.6 times the east force, correlates at −0.13 to +0.27 between KKN and the teleseismic solutions, and the KKN north force departs from them where its vertical does, with the opposite sign (Fig. 2F). KKN lies south-southeast of the source, where a vertical and a north force excite similar Rayleigh waves. One station cannot separate them, and the trade-off accounts for both differences. Green's functions for the 50-km crust along the path instead of the 15-km crust of ak135f halve the KKN

force but do not remove these differences (Fig. S6). We therefore take the teleseismic solutions, which record the source along 28 paths, as the reference for both components.

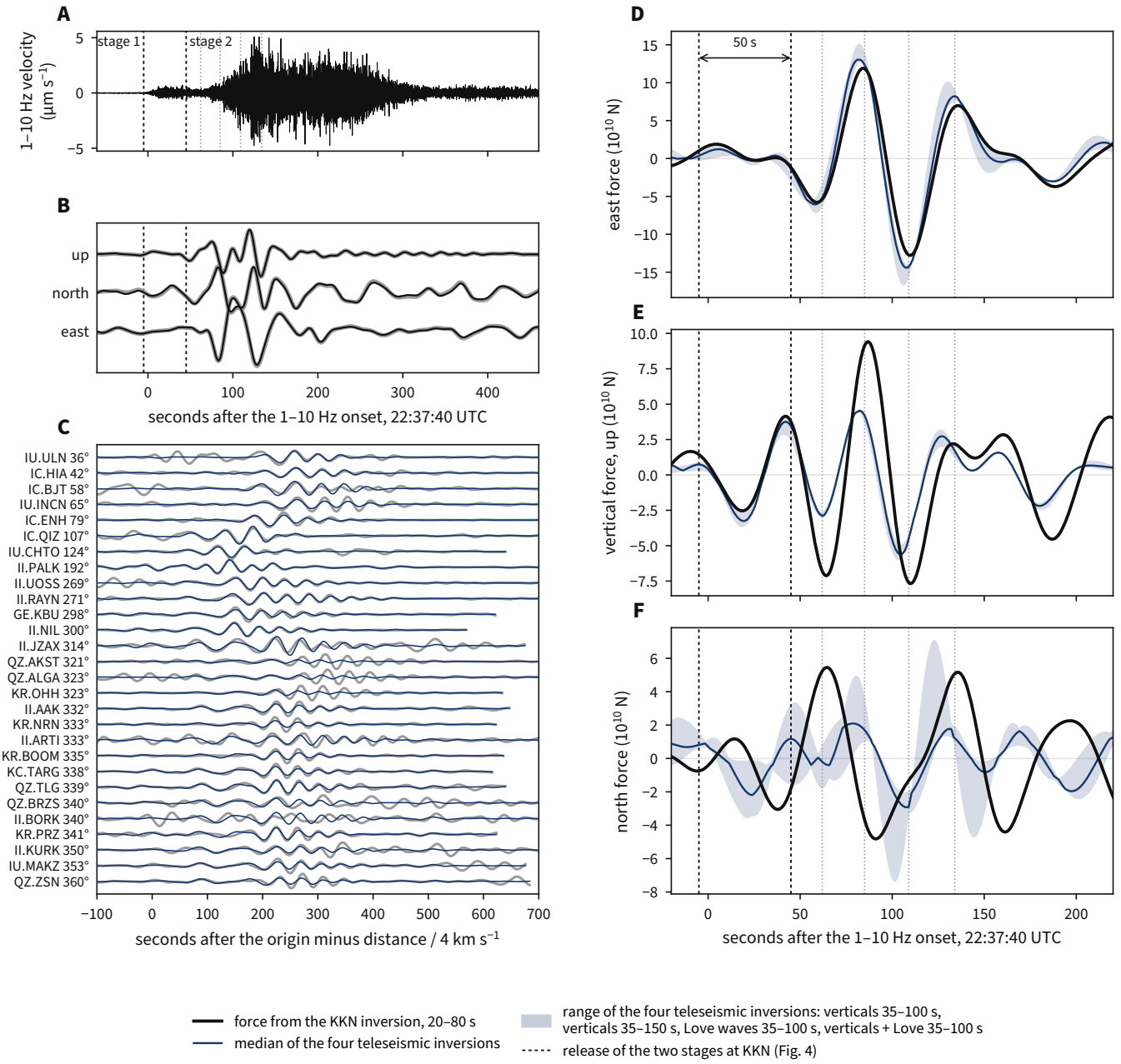



**Figure 2** The single-force inversions and their fit to the data. (A) NK.KKN vertical velocity at 1–10 Hz, with the release times of the two stages of the best simulation (dashed; Fig. 4) and the four force pulses (dotted). (B) NK.KKN displacement, 20–80 s, observed (gray) and synthetic from the KKN inversion (black). (C) The 28 teleseismic verticals, 35–100 s, by azimuth, labeled with station and azimuth, each normalized to its observed maximum, observed (gray) and synthetic from the corrected vertical inversion (blue), against time after the origin reduced by 4 km $s^{-1}$. (D) East, (E) vertical and (F) north force on the Earth in absolute time, 35–100 s, with ak135f functions, from the KKN inversion (black) and the four corrected teleseismic inversions, as their range (band) and median (blue line); E leaves out the Love-wave inversion. Dotted lines mark the KKN pulses of its 20–80 s solution and dashed lines the two releases, 50 s apart.

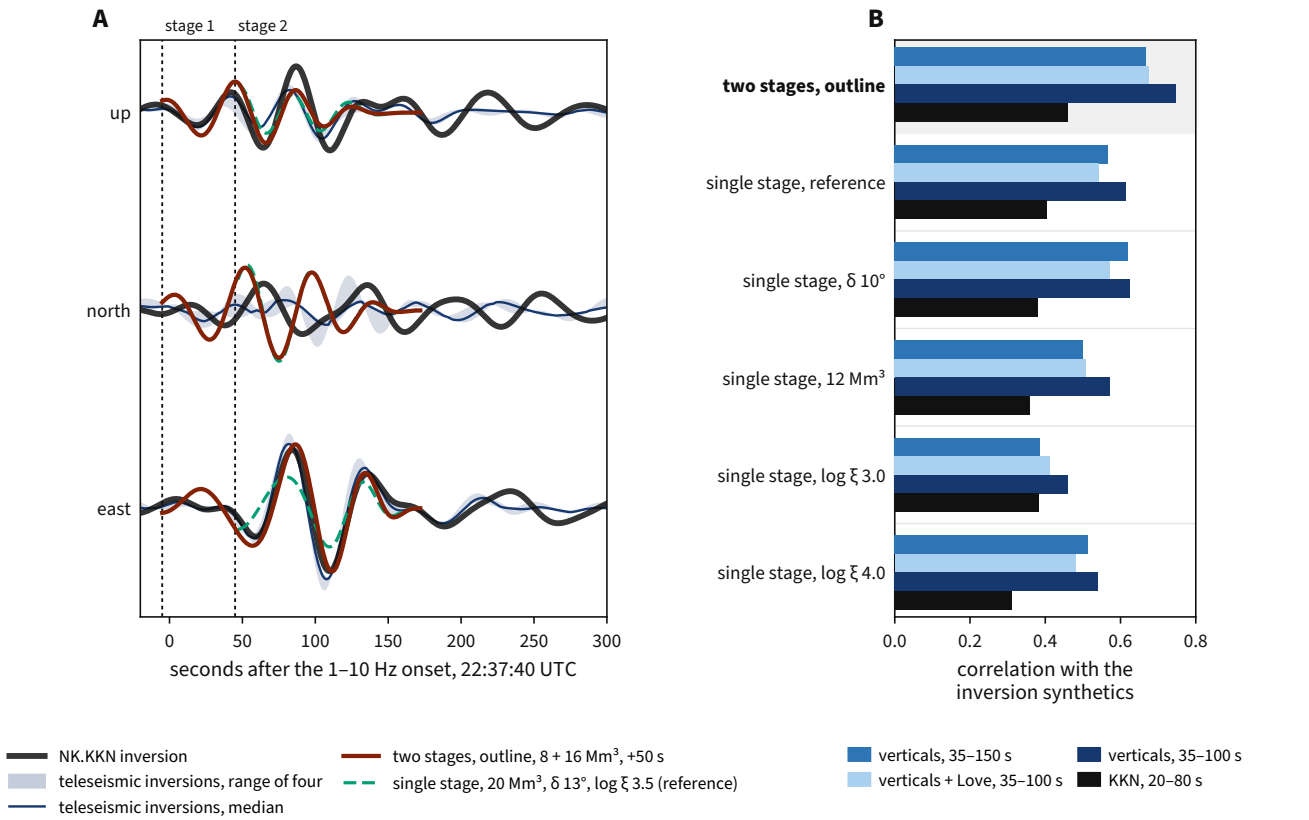



**Figure 3** Simulated forces from r.avaflow and their fit to the inversions. (A) Force on the Earth at 35–100 s from the KKN inversion (thick black), the four corrected teleseismic inversions (blue band, their range; blue line, their median) and two simulations, the best two-stage release and the single-stage reference, each simulated force from the KKN release time of its simulation until mass first leaves the grid; dashed lines mark the two releases of the best simulation, −5 and +45 s. (B) Score of each simulation, the correlation of its synthetics with those of the inversion, for the 35–150 s verticals, the verticals and horizontals at 35–100 s, the 35–100 s verticals and NK.KKN, each at its own release time; the best two-stage simulation is shaded. The variance reduction of the data is about the square of this correlation times that of the inversion; for the two-stage simulation from the mapped outline it is 0.25, 0.17 and 0.29 on these teleseismic sets (inversions 0.56, 0.38 and 0.52) and 0.20 at KKN (0.90). Release times, PREM values, amplitude factors, implied masses and the KKN correlations are in Table S1.

## 3.2 Fit of the flow simulations to the force

Released in a single stage, 20 $Mm^3$ with a turbulent coefficient $\log_{10}\xi$ of 3.5 accelerates down the 50° face, impacts at its base, runs down the upper gorge and reaches the Shyar after 120 s at 90–120 $m\,s^{-1}$. Its force reproduces the four teleseismic inversions with correlations of 0.47–0.61 and the KKN east component at +0.60, and the data sets agree on its release time, +47 s after the onset at KKN and +40 to +45 s for the teleseismic inversions (Fig. 3, Table S1). The two-stage releases fit better. Released as 8 $Mm^3$ from the lower face and 16 $Mm^3$ from the upper face 42–50 s later, the simulation correlates at 0.52–0.72 with the four teleseismic inversions, with the KKN east component at +0.65 to +0.78. The same 8 + 16 $Mm^3$, released 50 s apart from the mapped outline, has the highest correlation of all 28 simulations, with teleseismic waveform and force-direction cor-

relations of 0.58–0.75 and 0.67–0.81 (Fig. 4). In the best fit to the five data sets, the first stage of this simulation, 8 $Mm^3$ from the lower face, is released at the onset (−12 to −5 s) and the second stage, 16 $Mm^3$ from the upper face, 50 s later at +38 to +45 s. The single-stage simulation, released at +40 to +47 s, models only the second stage and misses the first. The first stage reaches the base of the face at 60–62 s and makes the weak west-down pulse there (Fig. 4).

The fit depends mainly on the speed of the mass during the first two minutes. A $\log_{10}\xi$ of 3.5 fits better than 3.0 or 4.0 on each set and is the value at which the KKN east component and the release time agree. The agreement holds for near-source friction of 10–13° but not 16°, and for far-field friction of 2–3° but not 5°. The waveforms constrain the turbulent coefficient and both friction angles, whereas the volume changes the amplitude factor but not the fit.

Among the delays of the second stage, 50 s fits best, then 42 and 60 s. These delays put the main body's release at +38 to +47 s. The same 8 + 16 $Mm^3$, 50 s apart, released from the disc of Section 2.3 instead of the mapped outline fits the waveforms better but the force directions worse (Table S1).

### 3.3 The path of the mass

The best simulation reproduces all four pulses of the horizontal force (Fig. 4I). Its force vectors correlate at 0.61–0.81 with the five solutions. The four pulses correspond to the impact of the first stage at the base of the face and to the acceleration, impact and renewed acceleration of the main body down the face and the upper gorge. A single-stage simulation releases only the main body, so it reproduces the last three pulses but not the first (Fig. 3A). The mass moves south-southwest overall, but the path is deflected west into the Ungilung at the base of the face and back toward south at the bend; at periods of 35–100 s the sideways accelerations at the turns exceed those along the path, so the simulated force alternates east–west (Fig. 4I, J) and the pulses record the bends of the path. The axis of strongest 1–2 Hz radiation lies east–west while the simulated front descends the Ungilung, turns through northwest–southeast as the front passes the junction and lies north–south from 270 s, when the front runs west along the Shyar, following the normal to the direction of the front (Fig. 4K).

### 3.4 Mass from the amplitude factors

We obtain the mass from the amplitude factor (Section 2.3) times the simulated mass. For the four principal simulations, the single-stage reference, the two-stage releases at +42 and +50 s and

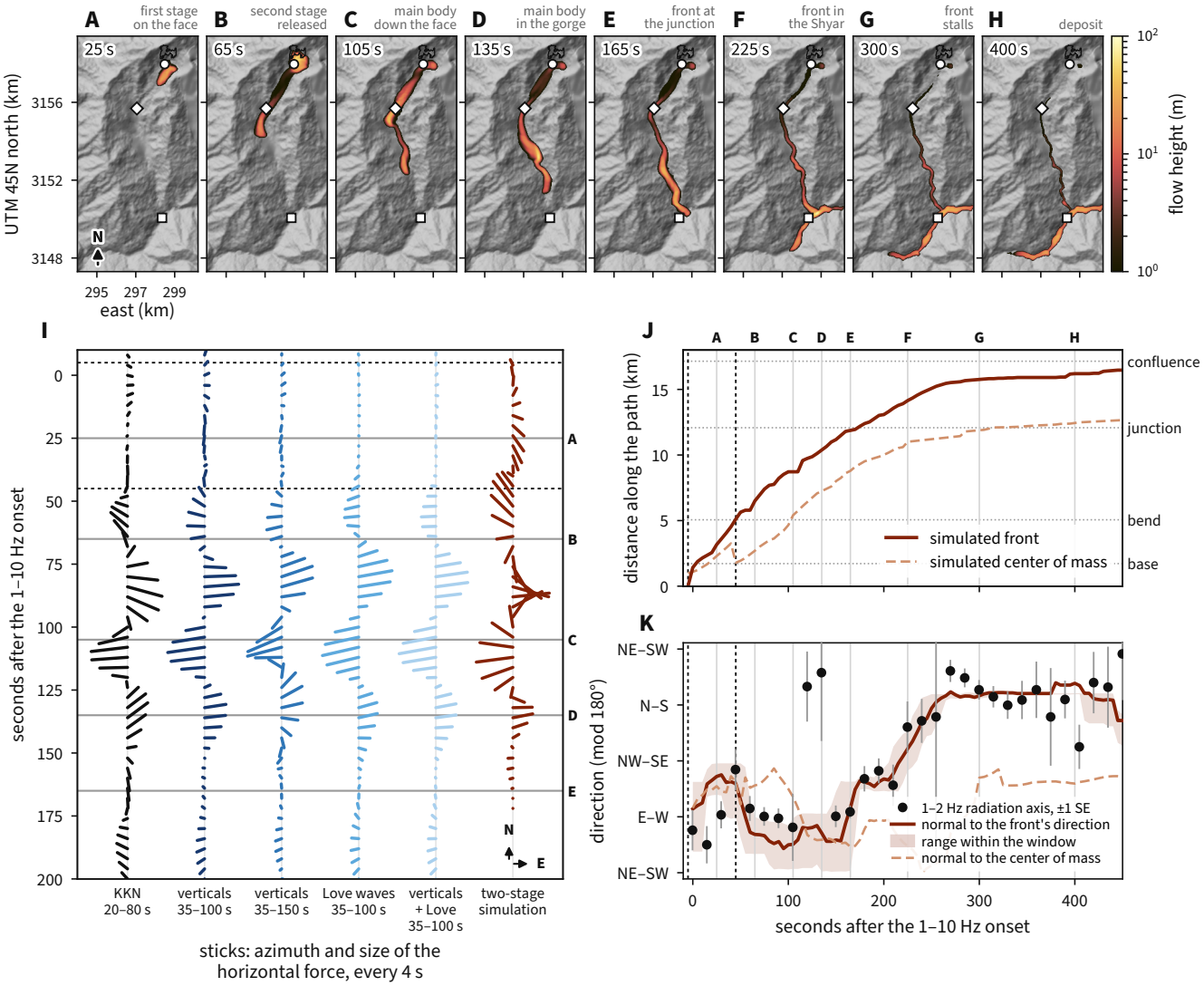



**Figure 4** The two-stage failure in the flow model. (A–H) Flow height of the best simulation, 8 $Mm^3$ from the lower and 16 $Mm^3$ from the upper face, the first at its KKN release time ($-5$ s) and the second 50 s later, continued for 900 s, at 25, 65, 105, 135, 165, 225, 300 and 400 s after the 1–10 Hz onset, on the GLO-30 hillshade with the release zones outlined, each panel labeled with its time and, above it, with the phase of the simulation, and the base of the face, the bend and the junction marked as in Fig. 1; gray lines in I, J and K mark these times and carry the panel letters. (I) The horizontal force on the Earth against time, 35–100 s, for the five corrected inversions and the simulation, one column each, as a stick every 4 s in the azimuth of the force (north up, east right) with a length proportional to $|F_h|$, scaled to the maximum of its row; the mass accelerates toward the azimuth plus 180°. (J) The simulated center of mass and front against time along the path of Fig. 1E, continued down the Shyar to the confluence, as slope distance, with the base of the face, the bend, the junction and the confluence named on the right; the front reaches the junction at 173 s and stalls 1.3 km above the confluence from 300 s, and the center of mass steps back when the second stage is released. (K) The axis of strongest 1–2 Hz radiation at nine near-field stations at 158–258° in azimuth (Section 2.1; Fig. S4), with one standard error, against the normal to the direction of the simulated front over the window, shaded over the range of the path normal within the window, and the normal to the direction of its center of mass, all modulo 180°. Dashed lines in I, J and K mark the release of the two stages.

the upper face first at +60 s (Table S1), the factor is 0.48–0.70 on the corrected 35–100 s verticals, 0.28–0.53 on the Love and combined sets and 0.59–0.87 at 35–150 s. At 2500 kg m$^{-3}$ these 20–24 Mm$^3$ simulations therefore imply 10–17, 6–13 and 12–21 Mm$^3$, respectively (Fig. S2), 6–21 Mm$^3$ in all. This is 17–47% of what the Ekström–Stark scaling gives for the peak force in each band, because the steep, direct path produces more force per unit mass than a gentler route. Spread over the 0.31 km$^2$ of face stripped of snow, a lower bound on the scar area, 6–21 Mm$^3$ would be at most 19–68 m deep on average. We leave the KKN value, 5–7 Mm$^3$, out of this range because Green's functions for the 50-km crust along its path (Laske et al., 2013) halve the force (Section 3.1; Fig. S6).

### 3.5 Robustness and limitations of the two-stage result

The two stages are inferred from the pulse at 60 s and from the release times, both of which depend on the corrected Green's functions. We computed synthetic records of single-stage simulations, added recorded noise and the phase errors that remain after the corrections, and inverted them as we inverted the data. For these single-stage records, the two-stage simulation fit better in at most 1% of 200 trials, and in no trial by as much as in the observed records. When the records came from a two-stage simulation instead, it fit better in 96–100% of trials (Fig. S5; Supplement S3). One error these trials cannot detect is a period-dependent delay shared by all stations, because it reshapes the force without changing the fit. The KKN record, which has no teleseismic corrections, and the surface-wave excitation of the calibration earthquakes in the local crust both indicate a delay of 0.93–1.05 times the value we applied. With the delay scaled to 0.75 or 1.25 of that value, the two-stage simulation fits better than the best single-stage simulation at 35–100 s (Supplement S3). A third test uses the amplitude spectrum at KKN, which phase errors do not change because both failure stages share the path to it. The two-stage simulation matches the spectral shape better than any single-stage simulation.

The speed of the mass and its division between failure stages are less well constrained. The speed between the pulses, 60–120 m s$^{-1}$, depends on the flow physics and on the 2–8 Hz envelope at KKN, which lasts until 250 s. The 2–8 Hz energy of the first 60 s is about 2% of that of the four pulses (Fig. S4C), which suggests a smaller first stage or one that radiated less energy. Either the upper or the lower face may have failed first, since the simulation that releases the upper face 60 s ahead of the lower fits as well (Table S1).

## 4 Conclusions

The Budhi Gandaki avalanche left the south face of the Chamar massif in two stages, a smaller one at the onset of the high-frequency signal and the main body 40–60 s later, with a total volume of 6–21 $Mm^3$. The force alternates between east and west in both the regional and the teleseismic solutions, and with the path corrections its polarity shows a mass moving westward. Neither result depends on a flow model, whereas the interpretation of the pulses does. The mass moved southwest and then south at 60–120 $m\,s^{-1}$ and reached the Shyar within three minutes, when the 1–2 Hz radiation axis turns with the front (Fig. 4K), and dammed it. The deposit filled the valley 2 km upstream, consistent with post-event imagery (Fig. S7) and field reports (National Disaster Risk Reduction and Management Authority (NDRRMA), 2026).

With three-dimensional path corrections, open teleseismic records can resolve the force histories of other large Himalayan landslides.

## Acknowledgements

We thank the National Seismological Centre of Nepal for keeping the Kakani station open, the operators of all the networks whose records we used, and the EarthScope and GEOFON data centers for serving them. Data were accessed from the NSF NGF data archive operated by EarthScope Consortium (NSF award 2435260). We thank Dan Shugar and Nawaraj Parajuli for posting their satellite comparisons of the source within days of the event, the Center for Land Surface Hazards for its StoryMap of the event, and the National Disaster Risk Reduction and Management Authority of Nepal for its report. We thank the developers of r.avaflow, Syngine, AxiSEM and REM3D for making their tools and models openly available, and the U.S. Geological Survey and the European Space Agency for open Landsat and Sentinel data. We used Claude (Anthropic) to assist with code and to format the manuscript in LaTeX. We checked all code, results, and text and take full responsibility for the content.

## Data and code availability

Waveforms and station metadata were obtained through the EarthScope, GEOFON and Raspberry Shake FDSN web services for networks NK (National Seismological Centre, 1978), II (EarthScope Consortium, 1986), IU (Albuquerque Seismological Laboratory/USGS, 1988), IC (Albuquerque Seis-

mological Laboratory (ASL)/USGS, 1992), KR (Kyrgyz Institute of Seismology, KIS, 2007), KC (Central Asian Institute for Applied Geosciences, 2008), QZ (Seismological Experience and Methodology Expedition of the Committee of Science of the Ministry of Education and Science of the Republic of Kazakhstan, 2003), GE (GEOFON Data Centre, 1993) and AM (Raspberry Shake, S.A., 2016); the near-field stations of Figs. 4K and S4 are listed in the archive. Green's functions were computed with Syngine (IRIS DMC, 2015; Krischer et al., 2017) from the AxiSEM (Nissen-Meyer et al., 2014) databases for ak135f and PREM, and with pyprop8 (O'Toole and Woodhouse, 2011; Valentine and Sambridge, 2022) for CRUST1.0 (Laske et al., 2013; Fig. S6); the path corrections use REM3D (Moulik et al., 2021; Moulik, 2022), and the calibration synthetics Mineos (Masters et al., 2011) with Global CMT and USGS moment tensors (Dziewonski et al., 1981; Ekström et al., 2012). The elevation models are Copernicus GLO-30 and GLO-90 (European Space Agency and Airbus, 2022), produced using Copernicus WorldDEM-30 and WorldDEM-90 © DLR e.V. 2010–2014 and © Airbus Defence and Space GmbH 2014–2018, provided under COPERNICUS by the European Union and ESA, all rights reserved. The imagery is Sentinel-2 L2A (European Space Agency, 2022) and Landsat 9 (Earth Resources Observation and Science (EROS) Center, 2020), the rivers OpenStreetMap data (© OpenStreetMap contributors, Open Database License); the public PlanetScope comparison (Shugar, 2026), © 2026 Planet Labs PBC, is neither reproduced nor redistributed. The flow simulations used r.avaflow 3 (Mergili et al., 2017; Mergili and Pudasaini, 2023) and the seismic analysis ObsPy (Krischer et al., 2015). The analysis code and derivative products are archived on Zenodo (Calvelage et al., 2026). The derived data are under the CC BY 4.0 license and the code under the GNU General Public License, version 3 or later.

## Competing interests

This work was supported by the NSF National Geophysical Facility (NSF NGF), operated by EarthScope Consortium under NSF award 2435260. Any opinions, findings and conclusions, or recommendations expressed in this material do not necessarily reflect the views of the U.S. National Science Foundation. We declare no competing interests.

## References

Adhikari, L. B., Subedi, S., Hetényi, G., Bollinger, L., Li, L., Hicks, S. P., Karplus, M. S., Diaz, J., Thapa, H. R., Pokharel, T., Timsina, C., Poudel, A., Pokhrel, K., Bhattarai, S., Weiskopf, E., Sharma, R., and Bhattarai, M. Tsangbu Ri

slope failure triggers massive flash flood across the Himalaya and shakes the globe – the seismic observations. *Seismica*, 5(2), 2026. doi: 10.26443/seismica.v5i2.3433.

Albuquerque Seismological Laboratory (ASL)/USGS. New China Digital Seismograph Network [Data set]. International Federation of Digital Seismograph Networks, 1992. doi: 10.7914/SN/IC.

Albuquerque Seismological Laboratory/USGS. Global Seismograph Network (GSN - IRIS/USGS) [Data set]. International Federation of Digital Seismograph Networks, 1988. doi: 10.7914/SN/IU.

Allstadt, K. Extracting source characteristics and dynamics of the August 2010 Mount Meager landslide from broadband seismograms. *Journal of Geophysical Research: Earth Surface*, 118(3):1472–1490, 2013. doi: 10.1002/jgrf.20110.

Calvelage, C. M., Huang, S., Chen, C.-M., Wang, B., Pratt-Sitaula, B., and McLaughlin, J. M. Dataset for: Seismic evidence for a two-stage origin of the October 2026 Budhi Gandaki landslide in the Nepal Himalaya [Data set]. Zenodo, 2026. doi: 10.5281/zenodo.24143591.

Central Asian Institute for Applied Geosciences. Central Asian Seismic Network of CAIAG [Data set]. International Federation of Digital Seismograph Networks, 2008. doi: 10.7914/SN/KC.

Chao, W.-A., Zhao, L., Chen, S.-C., Wu, Y.-M., Chen, C.-H., and Huang, H.-H. Seismology-based early identification of dam-formation landquake events. *Scientific Reports*, 6(1):19259, 2016. doi: 10.1038/srep19259.

Dziewonski, A. M. and Anderson, D. L. Preliminary reference Earth model. *Physics of the Earth and Planetary Interiors*, 25(4):297–356, 1981. doi: 10.1016/0031-9201(81)90046-7.

Dziewonski, A. M., Chou, T.-A., and Woodhouse, J. H. Determination of earthquake source parameters from waveform data for studies of global and regional seismicity. *Journal of Geophysical Research: Solid Earth*, 86(B4): 2825–2852, 1981. doi: 10.1029/JB086iB04p02825.

Earth Resources Observation and Science (EROS) Center. Landsat 8-9 Operational Land Imager / Thermal Infrared Sensor Level-1, Collection 2 [Data set]. U.S. Geological Survey, 2020. doi: 10.5066/P975CC9B.

EarthScope Consortium. Global Seismograph Network - II [Data set]. International Federation of Digital Seismograph Networks, 1986. doi: 10.7914/SN/II.

Ekström, G. and Stark, C. P. Simple scaling of catastrophic landslide dynamics. *Science*, 339(6126):1416–1419, 2013. doi: 10.1126/science.1232887.

Ekström, G., Nettles, M., and Dziewoński, A. M. The global CMT project 2004–2010: Centroid-moment tensors for 13,017 earthquakes. *Physics of the Earth and Planetary Interiors*, 200–201:1–9, 2012. doi: 10.1016/j.pepi.2012.04.002.

European Space Agency. Sentinel-2 MSI Level-2A BOA Reflectance [Data set], 2022. doi: 10.5270/S2_-znk9xsj.

European Space Agency and Airbus. Copernicus DEM – Global and European Digital Elevation Model (COP-DEM) [Data set], 2022. doi: 10.5270/ESA-c5d3d65.

Fukao, Y. Single-force representation of earthquakes due to landslides or the collapse of caverns. *Geophysical Journal International*, 122(1):243–248, 1995. doi: 10.1111/j.1365-246X.1995.tb03551.x.

GEOFON Data Centre. GEOFON Seismic Network [Data set]. GFZ Data Services, 1993. doi: 10.14470/TR560404.

Hancox, G. T., McSaveney, M. J., Manville, V. R., and Davies, T. R. The October 1999 Mt Adams rock avalanche and subsequent landslide dam-break flood and effects in Poerua River, Westland, New Zealand. *New Zealand Journal of Geology and Geophysics*, 48(4):683–705, 2005. doi: 10.1080/00288306.2005.9515141.

Hibert, C., Ekström, G., and Stark, C. P. Dynamics of the Bingham Canyon Mine landslides from seismic signal analysis. *Geophysical Research Letters*, 41(13):4535–4541, 2014. doi: 10.1002/2014GL060592.

Huang, S., Chen, C.-M., and Wang, B. Datasets and analysis scripts for "The first minutes of the 2026 Nepal rock–ice avalanche and flash flood" [Data set]. Zenodo, 2026. doi: 10.5281/zenodo.22884627.

IRIS DMC. Data Services Products: Syngine [Data set]. Incorporated Research Institutions for Seismology, 2015. doi: 10.17611/DP/SYNGINE.1.

Kanamori, H. and Given, J. W. Analysis of long-period seismic waves excited by the May 18, 1980, eruption of Mount St. Helens—A terrestrial monopole? *Journal of Geophysical Research: Solid Earth*, 87(B7):5422–5432, 1982. doi: 10.1029/JB087iB07p05422.

Kennett, B. L. N., Engdahl, E. R., and Buland, R. Constraints on seismic velocities in the Earth from traveltimes. *Geophysical Journal International*, 122(1):108–124, 1995. doi: 10.1111/j.1365-246X.1995.tb03540.x.

Krischer, L., Megies, T., Barsch, R., Beyreuther, M., Lecocq, T., Caudron, C., and Wassermann, J. ObsPy: A bridge for seismology into the scientific Python ecosystem. *Computational Science & Discovery*, 8(1):014003, 2015. doi: 10.1088/1749-4699/8/1/014003.

Krischer, L., Hutko, A. R., van Driel, M., Stähler, S., Bahavar, M., Trabant, C., and Nissen-Meyer, T. On-demand custom broadband synthetic seismograms. *Seismological Research Letters*, 88(4):1127–1140, 2017. doi: 10.1785/0220160210.

Kyrgyz Institute of Seismology, KIS. Kyrgyz Digital Network [Data set]. International Federation of Digital Seismograph Networks, 2007. doi: 10.7914/SN/KR.

Laske, G., Masters, G., Ma, Z., and Pasyanos, M. Update on CRUST1.0 – A 1-degree Global Model of Earth's Crust. In *Geophysical Research Abstracts*, volume 15. EGU General Assembly, 2013. Abstract EGU2013-2658.

Masters, G., Woodhouse, J. H., and Gilbert, F. Mineos v1.0.2 [Computer software]. Computational Infrastructure for Geodynamics, https://geodynamics.org/resources/mineos, 2011.

Mergili, M. and Pudasaini, S. P. r.avaflow – The mass flow simulation tool, version 3 (release 20230411) [Computer software]. https://www.avaflow.org, 2023.

Mergili, M., Fischer, J.-T., Krenn, J., and Pudasaini, S. P. r.avaflow v1, an advanced open-source computational framework for the propagation and interaction of two-phase mass flows. *Geoscientific Model Development*, 10 (2):553–569, 2017. doi: 10.5194/gmd-10-553-2017.

Moretti, L., Allstadt, K., Mangeney, A., Capdeville, Y., Stutzmann, E., and Bouchut, F. Numerical modeling of the Mount Meager landslide constrained by its force history derived from seismic data. *Journal of Geophysical Research: Solid Earth*, 120(4):2579–2599, 2015. doi: 10.1002/2014JB011426.

Moretti, L., Mangeney, A., Walter, F., Capdeville, Y., Bodin, T., Stutzmann, E., and Le Friant, A. Constraining landslide characteristics with Bayesian inversion of field and seismic data. *Geophysical Journal International*, 221(2):1341–1348, 2020. doi: 10.1093/gji/ggaa056.

Moulik, P. Dataset for Global Reference Seismological Data Sets: Multimode Surface Wave Dispersion (v1.0) [Data set]. Zenodo, 2022. doi: 10.5281/zenodo.8371229.

Moulik, P., Lekic, V., Romanowicz, B., Ma, Z., Schaeffer, A., Ho, T., Beucler, E., Debayle, E., Deuss, A., Durand, S., Ekström, G., Lebedev, S., Masters, G., Priestley, K., Ritsema, J., Sigloch, K., Trampert, J., and Dziewonski, A. M. Global reference seismological data sets: multimode surface wave dispersion. *Geophysical Journal International*, 228(3):1808–1849, 2021. doi: 10.1093/gji/ggab418.

National Disaster Risk Reduction and Management Authority (NDRRMA). An avalanche and massive landslide triggered the devastating Budhi Gandaki flood, report finds. Technical report as reported by OnlineKhabar, 13 October 2026, https://english.onlinekhabar.com/avalanche-landslide-budhi-gandaki-flood.html, 2026.

National Seismological Centre. Nepal Kathmandu [Data set]. International Federation of Digital Seismograph Networks, 1978. doi: 10.7914/SN/NK.

Nissen-Meyer, T., van Driel, M., Stähler, S. C., Hosseini, K., Hempel, S., Auer, L., Colombi, A., and Fournier, A. AxiSEM: broadband 3-D seismic wavefields in axisymmetric media. *Solid Earth*, 5(1):425–445, 2014. doi: 10.5194/se-5-425-2014.

O'Toole, T. B. and Woodhouse, J. H. Numerically stable computation of complete synthetic seismograms including the static displacement in plane layered media. *Geophysical Journal International*, 187(3):1516–1536, 2011. doi: 10.1111/j.1365-246X.2011.05210.x.

Petley, D. The 11 October 2026 landslide and debris flow/flood on the Budhi Gandaki River in Gorkha district, Nepal. The Landslide Blog, Eos, 12 October 2026, https://eos.org/thelandslideblog/the-11-october-2026-landslide-and-debris-flow-flood-on-the-budhi-gandaki-river-in-gorkha-district-nepal, 2026.

Raspberry Shake, S.A. Raspberry Shake [Data set]. International Federation of Digital Seismograph Networks,

2016. doi: 10.7914/SN/AM.

Seismological Experience and Methodology Expedition of the Committee of Science of the Ministry of Education and Science of the Republic of Kazakhstan. Seismic network of the Seismological Experience and Methodology Expedition CS MES RK [Data set]. International Federation of Digital Seismograph Networks, 2003. doi: 10.7914/SN/QZ.

Shugar, D. H. PlanetScope comparison of the Budhi Gandaki flood source, 1 and 14 October 2026. Bluesky post, https://bsky.app/profile/watershedlab.bsky.social/post/3mxtkwxdaok2u, 14 October 2026; imagery © 2026 Planet Labs PBC, 2026.

Shugar, D. H., Jacquemart, M., Shean, D., Bhushan, S., Upadhyay, K., Sattar, A., Schwanghart, W., McBride, S., de Vries, M. V. W., Mergili, M., Emmer, A., Deschamps-Berger, C., McDonnell, M., Bhambri, R., Allen, S., Berthier, E., Carrivick, J. L., Clague, J. J., Dokukin, M., Dunning, S. A., Frey, H., Gascoin, S., Haritashya, U. K., Huggel, C., Kääb, A., Kargel, J. S., Kavanaugh, J. L., Lacroix, P., Petley, D., Rupper, S., Azam, M. F., Cook, S. J., Dimri, A. P., Eriksson, M., Farinotti, D., Fiddes, J., Gnyawali, K. R., Harrison, S., Jha, M., Koppes, M., Kumar, A., Leinss, S., Majeed, U., Mal, S., Muhuri, A., Noetzli, J., Paul, F., Rashid, I., Sain, K., Steiner, J., Ugalde, F., Watson, C. S., and Westoby, M. J. A massive rock and ice avalanche caused the 2021 disaster at Chamoli, Indian Himalaya. *Science*, 373(6552): 300–306, 2021. doi: 10.1126/science.abh4455.

Valentine, A. P. and Sambridge, M. pyprop8: A lightweight code to simulate seismic observables in a layered half-space. *Journal of Open Source Software*, 7(76):4217, 2022. doi: 10.21105/joss.04217.

# Supplementary Material for: Seismic evidence for a two-stage origin of the October 2026 Budhi Gandaki landslide in the Nepal Himalaya

**Christopher M. Calvelage** * [1], **Shuye Huang** [2], **Chan-Mao Chen** [3], **Binhao Wang** [4], **Beth Pratt-Sitaula** [1], **J. Mitchell McLaughlin** [5]

[1]EarthScope Consortium, Washington, D.C., USA, [2]Earthquake Research Institute, The University of Tokyo, Tokyo, Japan, [3]Department of Earth Sciences, University of Southern California, Los Angeles, CA, USA, [4]Scripps Institution of Oceanography, University of California San Diego, La Jolla, CA, USA, [5]New Mexico Institute of Mining and Technology, Socorro, New Mexico, USA

**Contents** Sections S1–S3, Figures S1–S7 and Tables S1–S2.

## S1: Inversions and path corrections

On a 1-s grid, the force $F_j(t_k)$, $j$ up, north and east, predicts trace $i$ as

$$s_i(t) = \sum_{j,k} G_{ij}(t - t_k)\, F_j(t_k)\, \Delta t \approx d_i(t + \tau_i), \tag{S1}$$

where $G_{ij}$ are the Green's functions, $d_i$ the record and $\tau_i$ its time shift. The force vector $\mathbf{m}$ minimizes

$$\sum_i w_i^2 \left\|\mathbf{d}_i - \mathbf{G}_i\mathbf{m}\right\|^2 + \lambda^2 \left(\|\mathbf{m}\|^2 + \beta \left\|\mathbf{D}_2\mathbf{m}\right\|^2\right), \qquad w_i = \frac{1}{\mathrm{rms}(\mathbf{d}_i)\sqrt{n_i}}, \qquad \beta = \left(\frac{T_0}{2\pi\,\Delta t}\right)^4, \tag{S2}$$

where $n_i$ is the number of stations in the 30° sector of trace $i$ (1 at KKN), $\mathbf{D}_2$ the second-difference operator and $T_0 = 10$ s the period at which both penalties are equal; $\lambda$ is chosen at the L-curve corner.

*Corresponding author: chris.calvelage@earthscope.org

The teleseismic Green's functions are corrected per period, with Rayleigh delays on the vertical and radial components and Love delays on the transverse, by the factor

$$\hat{G}_{ij}(\omega)\, e^{-i\omega\left[\tau_i^{\mathrm{R}}(\omega)+\tau_i^{\mathrm{oc}}(\omega)+\tau_i^{\mathrm{cal}}(\omega)-\bar{\tau}\right]}, \qquad \tau_i^{\mathrm{R}} = -\frac{L_i}{c_0}\left\langle \frac{\delta c}{c} \right\rangle_i . \tag{S3}$$

The REM3D fundamental-mode phase anomalies (Moulik et al., 2021) were inverted at nine periods from 35 to 150 s for isotropic phase-velocity maps on 1442 spherical splines (Wang and Dahlen, 1995), damped at the L-curve corner, and averaged along the great circle of length $L_i$; $c_0$ is the phase velocity of PREM. The term $\tau^{\mathrm{oc}}$, from Mineos phase velocities (Masters et al., 2011), removes the 3-km ocean of PREM, which the REM3D reference has and the Syngine functions lack; for ak135f the measured delay of PREM relative to ak135f is added.

The delay $r_{ik}(T)$ left by the REM3D correction was measured for 14 earthquakes $k$ at each station $i$ at 48 periods from 35 to 150 s, and the correction is

$$\tau_i^{\mathrm{cal}}(T) = -\,w(T)\,\frac{\sum_k \omega_k\, r_{ik}(T)}{\sum_k \omega_k}, \qquad \omega_k = \frac{1}{d_k + 50\ \mathrm{km}}, \tag{S4}$$

where the sum runs over the earthquakes recorded over at least half of 35–75 s, $d_k$ is the distance of the earthquake from the source and $w(T)$ is a $\cos^2$ taper, 1 up to 60 s and 0 from 75 s. A station with fewer than three earthquakes takes the nearest correction within 4°, or else the network median. When each earthquake is predicted from the other 13, the corrections halve the error at 35–45 s (Rayleigh from 10 to 5 s at 35 s, Love from 8 to 6 s) and give no improvement above 65 s, so the taper ends at 75 s (Fig. S5C). Applied to the landslide records they raise the variance reduction of the 35–100 s verticals from 0.48 to 0.52.

For the force $\mathbf{m}$ of a simulation at a release time, the inverted force $\hat{\mathbf{m}}$ and $\mathbf{A} = \sum_i w_i^2\, \mathbf{G}_i^{\mathrm{T}}\mathbf{G}_i$, the correlation of the simulation's synthetics with the inversion's and the amplitude factor are

$$c = \frac{\mathbf{m}^{\mathrm{T}}\mathbf{A}\,\hat{\mathbf{m}}}{\sqrt{(\mathbf{m}^{\mathrm{T}}\mathbf{A}\,\mathbf{m})\,(\hat{\mathbf{m}}^{\mathrm{T}}\mathbf{A}\,\hat{\mathbf{m}})}}, \qquad a = \frac{\mathbf{m}^{\mathrm{T}}\mathbf{A}\,\hat{\mathbf{m}}}{\mathbf{m}^{\mathrm{T}}\mathbf{A}\,\mathbf{m}}, \tag{S5}$$

at the release time that maximizes $c$. The implied mass is $a\rho V$, with $V$ the simulation's volume and $\rho$ = 2500 kg m$^{-3}$.

## S2: Satellite imagery

The outline was mapped from a public comparison of PlanetScope scenes of 1 and 14 October 2026 (Shugar, 2026), posted as a swipe video, from whose frames co-registered mosaics of both dates were assembled for four views. Each 1 October mosaic was matched to the Sentinel-2 L2A scene of that day with SIFT features and a RANSAC similarity transform (7 m rms, 2.0–2.6 m per screen pixel), and three views were warped to a 2.5-m UTM grid. Two classes of change were mapped inside the Ungilung catchment from the gray-level brightness of the two dates, scaled to 0–1. Strong darkening requires a brightness above 0.55 on 1 October and below 0.45 on 14 October. Snow loss requires the same brightness on 1 October and, on 14 October, either a brightness below 0.72 or a red–blue chromaticity above 0.06, the brown visible through the haze over the face. The outline denotes changes rather than the failure plane. Cloud-free Sentinel-2 L2A scenes of 21, 23 and 26 October are consistent with it (Fig. S3C).

## S3: Phase errors of the Green's functions and the two-stage preference

We test whether the phase errors the corrections miss (Section S1) can produce the two-stage preference. Synthetic records of a simulation at its release time, scaled to the data, used Green's functions delayed station by station by the delay of an earthquake drawn at random in each trial minus the correction predicted from the other 13, pooled with the nearest stations. Phase-randomized pre-event noise was added, the records were inverted with the data's weights, regularization and $\pm$3 s station shifts, and the 19 single-stage and lower-first simulations were compared with the result as in Table S1. The sources were the six $\log_{10}\xi = 3.5$ single-stage simulations, each removed from the candidates, and the two-stage simulation at +50 s of Table S1. The correlation difference is the best two-stage minus the best single-stage correlation, positive when the two-stage simulation fits better (Section 3.5). At 35–100 s the correlation difference for the two-stage source, 0.04–0.08, falls short of the observed 0.10, which an error-free two-stage source reaches in 1–9% of trials.

These trials cannot detect a bias shared by all 14 earthquakes, because it is expressed as a delay common to all stations, which Table S2 tests. That delay, $m(T)$, is the mean over a set's stations of the delay applied to the Green's functions (the bracket of Eq. S3 without $\bar{\tau}$), minus its average over the band. For the 35–100 s verticals with ak135f it is +39, 0, $-20$ and $-24$ s at 35, 50, 75 and

100 s. Table S2 scales it by $\alpha$ at each station and leaves $\bar{\tau}$ and the differences between stations unchanged.

The excitation-pattern rows apply a delay that the corrections carry over from the earthquakes. The Rayleigh excitation of an earthquake at depth, computed from Mineos fundamental modes with CRUST1.0, differs in phase from that in PREM, whereas a surface force's does not, so the corrections pass the earthquakes' phase shift to the landslide. Through the estimator of Eq. S4 this shift becomes a delay at each station, 2.5–3.8 s rms at 35 s about its mean over the stations, and that mean is its contribution to $m(T)$. In ten versions of the calculation, which vary the source depth and the handling of near-nodal radiation, it is −0.4 to +1.4 s at 35 s, equivalent to $\alpha$ = 0.97–1.03 for the 35–100 s set and 0.95–1.05 for the 35–150 s set.

At KKN both stages share the path, so the amplitude spectrum is unaffected by phase errors. The spectral misfit of a simulation is

$$\Phi = \sum_b \left(\ell_b - \bar{\ell}\right)^2, \qquad \ell_b = \frac{1}{3}\sum_c \log_{10}\frac{|D_c|_b}{|S_c|_b}, \tag{S6}$$

over seven bins $b$ from 20 to 80 s and the three components $c$, where $|D|$ and $|S|$ are the amplitude spectra of the record and the simulation and $\bar{\ell}$ is the mean over bins; it was calibrated with pseudo-records of simulations plus real KKN noise.

**Table S1** Scores of twelve of the 28 simulations, including three released from the mapped outline (Fig. S3), one of them at the design thickness (thin outline), and two with the upper face released first (the other two-stage simulations release the lower face first), on the corrected teleseismic sets (REM3D and the calibration earthquakes, Section S1) and at NK.KKN. The correlation is that of the simulation's teleseismic synthetics with the inversion's, with ak135f Green's functions and the PREM value in parentheses. The KKN columns give the variance reduction at the best amplitude and the correlation of the simulated with the inverted east force. Release times are absolute (seconds after the 1–10 Hz onset); the teleseismic range spans the four sets. Amplitude factors are the factors by which the simulation's synthetics must be multiplied to match the inversion's, in the order 35–100 s verticals, 35–150 s verticals, Love waves, verticals + horizontals; the implied mass is the released volume times the factor at 2500 kg m$^{-3}$. With the upper face first at +40, +70 or +80 s, or with the larger stage first, the simulations correlate at 0.45–0.53 (mean of the four teleseismic correlations, against 0.64 at +60 s and 0.65 for the lower face first at +50 s). The scores, release times, runouts and implied masses of all 28 simulations, with one-dimensional, REM3D and fully corrected Green's functions, are in the files cal_summary.md, order/cal_summary.md and table_south.json of the Zenodo archive.

| simulation | $V$ (Mm$^3$) | $\log_{10}\xi$ | $\delta$ (°) | Z 35–100 | Z 35–150 | Love | Z + H | KKN VR | KKN cc$_E$ | rel. KKN (s) | rel. tele. (s) | amplitude factors | mass (Mm$^3$) |
|---|---|---|---|---|---|---|---|---|---|---|---|---|---|
| two stages, +50 s | 8 + 16 | 3.5 | 13/3 | 0.72 (0.71) | 0.65 (0.65) | 0.55 (0.52) | 0.65 (0.60) | 0.19 | +0.78 | -5 | [-10, -5] | 0.57/0.67/0.34/0.42 | 8–16 |
| two stages, +42 s | 8 + 16 | 3.5 | 13/3 | 0.66 (0.64) | 0.59 (0.59) | 0.52 (0.48) | 0.59 (0.54) | 0.20 | +0.65 | +2 | [-4, 0] | 0.48/0.59/0.28/0.35 | 7–14 |
| two stages, +60 s | 8 + 16 | 3.5 | 13/3 | 0.65 (0.61) | 0.59 (0.57) | 0.50 (0.48) | 0.60 (0.56) | 0.19 | +0.43 | -16 | [-18, -13] | 0.58/0.61/0.39/0.47 | 9–15 |
| upper face first, +60 s | 8 + 16 | 3.5 | 13/3 | 0.70 (0.69) | 0.64 (0.64) | 0.57 (0.54) | 0.65 (0.60) | 0.16 | +0.73 | -10 | [-16, -12] | 0.70/0.87/0.43/0.53 | 10–21 |
| upper face first, +50 s | 8 + 16 | 3.5 | 13/3 | 0.61 (0.59) | 0.55 (0.54) | 0.51 (0.48) | 0.56 (0.52) | 0.18 | +0.10 | +44 | [-10, -6] | 0.51/0.68/0.32/0.38 | 8–16 |
| outline, +50 s (Fig. 4) | 8 + 16 | 3.5 | 13/3 | 0.75 (0.73) | 0.67 (0.67) | 0.58 (0.56) | 0.67 (0.63) | 0.20 | +0.72 | -5 | [-12, -8] | 0.56/0.65/0.35/0.43 | 8–16 |
| outline centroid, +50 s | 8 + 16 | 3.5 | 13/3 | 0.79 (0.77) | 0.70 (0.69) | 0.61 (0.58) | 0.72 (0.67) | 0.21 | +0.65 | -4 | [-8, -5] | 0.61/0.66/0.39/0.48 | 9–16 |
| thin outline, +50 s | 2 + 6 | 3.5 | 13/3 | 0.57 (0.55) | 0.49 (0.49) | 0.51 (0.47) | 0.55 (0.51) | 0.13 | +0.36 | -6 | [-12, -8] | 1.21/1.31/0.87/0.99 | 7–11 |
| single stage, reference | 20 | 3.5 | 13/3 | 0.61 (0.59) | 0.57 (0.56) | 0.47 (0.43) | 0.54 (0.49) | 0.17 | +0.60 | +47 | [+40, +45] | 0.51/0.60/0.30/0.37 | 6–12 |
| single stage, 12 Mm$^3$ | 12 | 3.5 | 13/3 | 0.57 (0.55) | 0.50 (0.50) | 0.44 (0.41) | 0.51 (0.47) | 0.14 | +0.47 | +46 | [-10, +44] | 0.78/0.86/0.48/0.59 | 6–10 |
| single stage, $\log_{10}\xi$ 3.0 | 20 | 3.0 | 13/3 | 0.46 (0.45) | 0.39 (0.39) | 0.37 (0.34) | 0.41 (0.38) | 0.15 | -0.19 | +92 | [+36, +40] | 0.50/0.54/0.32/0.37 | 6–11 |
| single stage, $\log_{10}\xi$ 4.0 | 20 | 4.0 | 13/3 | 0.54 (0.52) | 0.51 (0.50) | 0.44 (0.42) | 0.48 (0.44) | 0.11 | -0.09 | +91 | [+40, +49] | 0.39/0.46/0.26/0.30 | 5–9 |

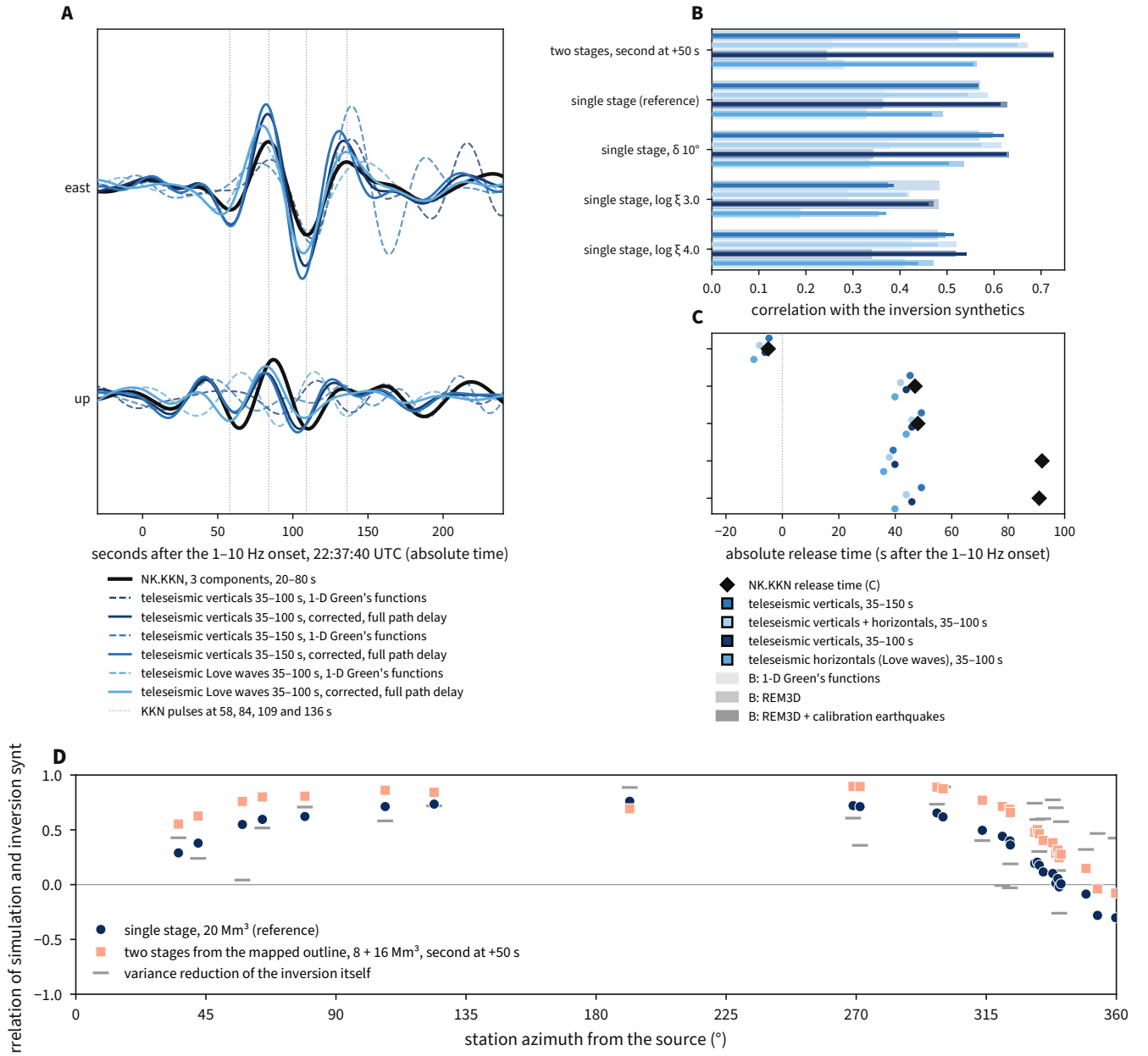



**Figure S1** Effect of the path corrections and the fit by station. (A) East and vertical force on the Earth, 35–100 s, in absolute time, from NK.KKN and from the teleseismic solutions with one-dimensional Green's functions (dashed) and with the corrected functions including the full path delay (solid; REM3D and the calibration earthquakes, Section S1), for the 35–100 s verticals, the 35–150 s verticals and the Love waves, with PREM functions; dotted lines mark the KKN pulses in this band. The mean delay over the station set, $\bar{\tau}$ in Eq. S3, +15 s for PREM and +26 s for ak135f at 35–100 s, translates the force in time; the corrected functions remove it and the absolute-time solutions keep it. (B) Correlation of the teleseismic synthetics of five simulations with the inversion synthetics on the four data sets, with one-dimensional (wide, light), REM3D (middle) and fully corrected (narrow, dark) functions. (C) Absolute release time of each simulation from the four teleseismic sets and from KKN (diamonds); the dotted line is the 1–10 Hz onset. (D) Correlation of the 35–100 s vertical synthetics of the single-stage reference and of the best two-stage simulation (released from the mapped outline, Fig. 4) with those of the corrected vertical inversion, by station azimuth, at each simulation's release time; gray ticks give the variance reduction of the inversion at each station. Nineteen of the 28 stations lie between 270° and 360°. Widening the station shifts of the inversion from ±3 to ±15 s adds 0.03 to its variance reduction and moves 24 of the 28 stations by less than 10 s; the other four are among the worst fitted, so the remaining misfit lies mostly in amplitude and waveform rather than in timing.

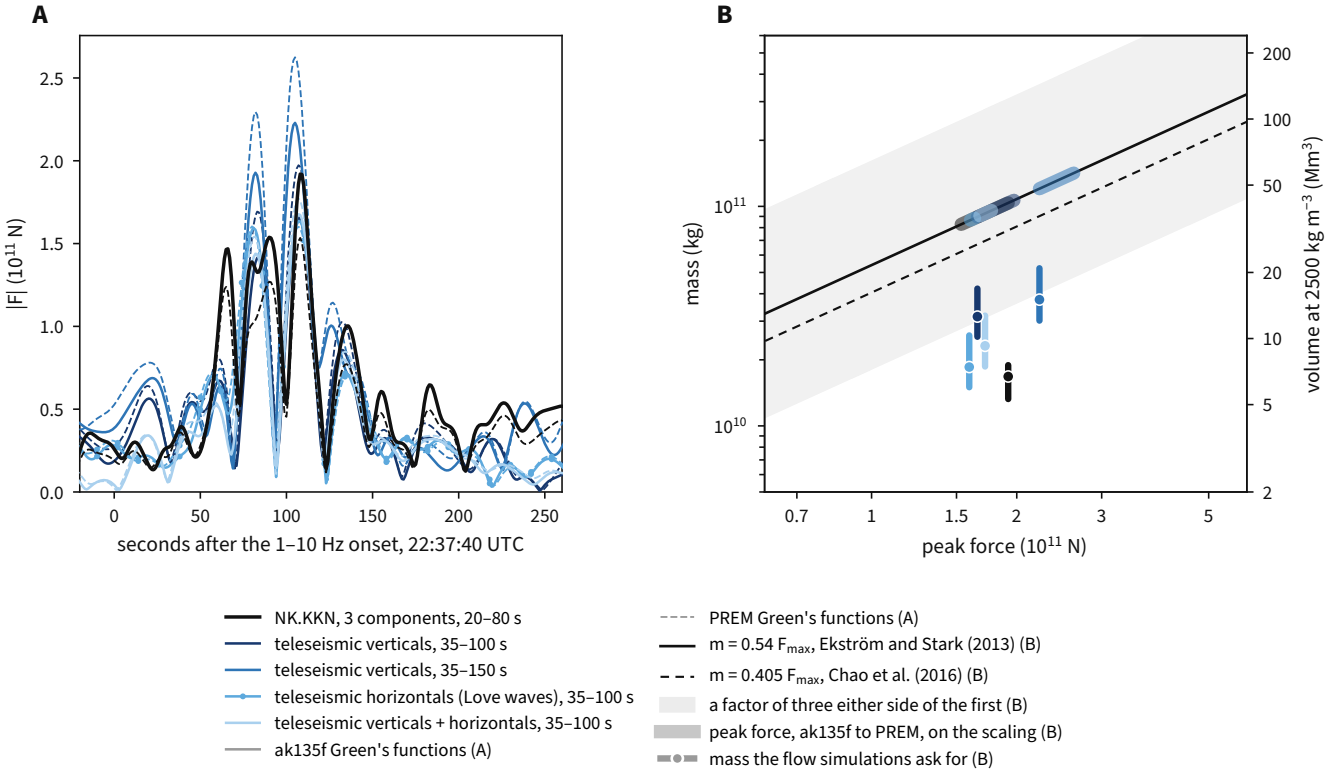



**Figure S2** Force and mass. (A) Magnitude of the force on the Earth from the KKN inversion and the four corrected teleseismic inversions in absolute time, with ak135f (solid) and PREM (dashed) functions. (B) Peak force against mass, with the scaling $m = 0.54\,F_{max}$ of Ekström and Stark (2013), a factor of three on either side, and $m = 0.405\,F_{max}$ of Chao et al. (2016); the peak force of each solution on the first scaling, from ak135f to PREM functions; and, at its ak135f peak force, the mass that the four principal simulations (the single-stage reference, the two-stage releases at +42 and +50 s and the upper face first at +60 s; Table S1) imply for each data set, the amplitude factor times the simulated mass (bars, dots at the medians; the Love and combined sets are offset by 2.5% in force). The KKN bar uses ak135f functions; functions for the crust along its path halve it (Fig. S6), and we leave KKN out of the mass range. The outline release of Fig. 4 implies 8–16 Mm$^3$ (Table S1), within these bars. The right axis gives the volume at 2500 kg m$^{-3}$.

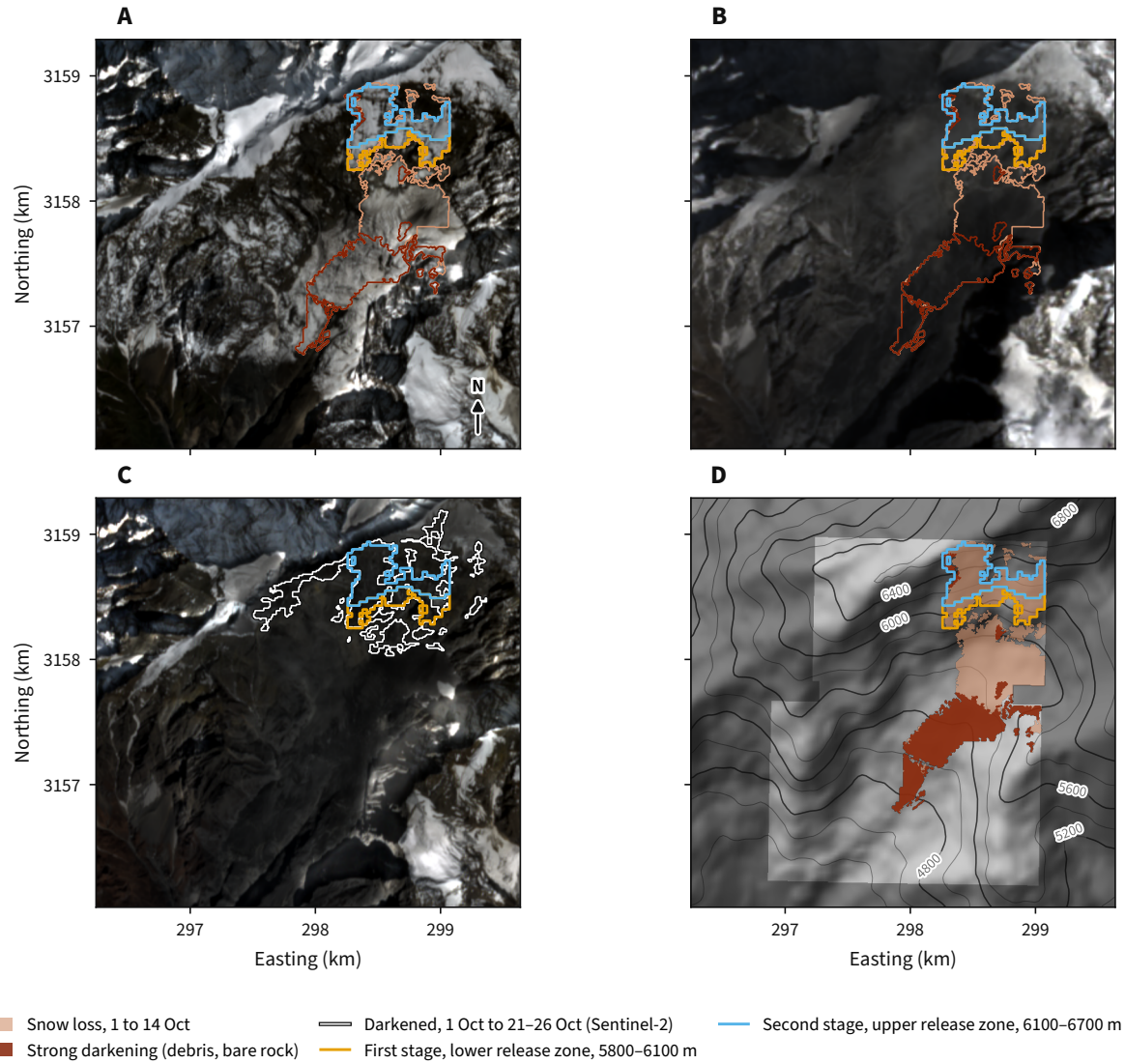



**Figure S3** Imagery of the flood source area. (A) Sentinel-2 L2A, 1 October 2026, true color, 10 m. (B) Landsat 9 Collection 2 Level-1, 13 October 2026, top-of-atmosphere true color pan-sharpened to 15 m, with thin cirrus over the face; image courtesy of the U.S. Geological Survey (Earth Resources Observation and Science (EROS) Center, 2020). On the Sentinel-2 scene of 6 October, 64% of the snow-loss area on the face and 79% of the darkened area on the glacier (D) were still snow-covered; on this Landsat scene 14% of the darkened area reads as snow against 87% at the same elevations elsewhere, and on the face, under the cirrus, 41% against 81%. (C) Sentinel-2 L2A, 26 October 2026, true color, 10 m, with the area near the face, on south-facing slopes steeper than 30° above 5400 m, whose green reflectance fell from above 0.3 on 1 October to below 0.15 in the median of the cloud-free scenes of 21, 23 and 26 October. On these scenes the green reflectance is below 0.15 on 87–92% of the snow-loss area on the face, against 4% on 1 October, 19% on 6 October and 32% on 21 October 2025, and on 83–88% of the lower and 91–94% of the upper release zone; the darkening ends between 6600 and 6800 m at the top of that area, and the darkened snowfield west of the face lies outside the Ungilung catchment. (D) The two classes of change mapped from the public PlanetScope comparison of 1 and 14 October (Shugar, 2026; Section S2) on the GLO-30 hillshade with 200-m contours labeled in meters, veiled outside the views of the comparison, namely snow loss, snow on 1 October that is dark or brown on 14 October (0.31 km$^2$ on the face at 5813–6735 m, mean slope 51°, 90% inside the two release zones; 0.71 km$^2$ on the lower slopes and the glacier) and strong darkening (0.31 km$^2$ of debris on the glacier at 4706–5469 m; 0.31–0.52 km$^2$ for thresholds of 0.40–0.50). The release zones of the two stages of the best simulation (Fig. 4) are drawn on all panels and the outlines of the two classes of D on A and B; each image is stretched to its own 1–99.5% range per band. The PlanetScope frames, © 2026 Planet Labs PBC, are not reproduced.

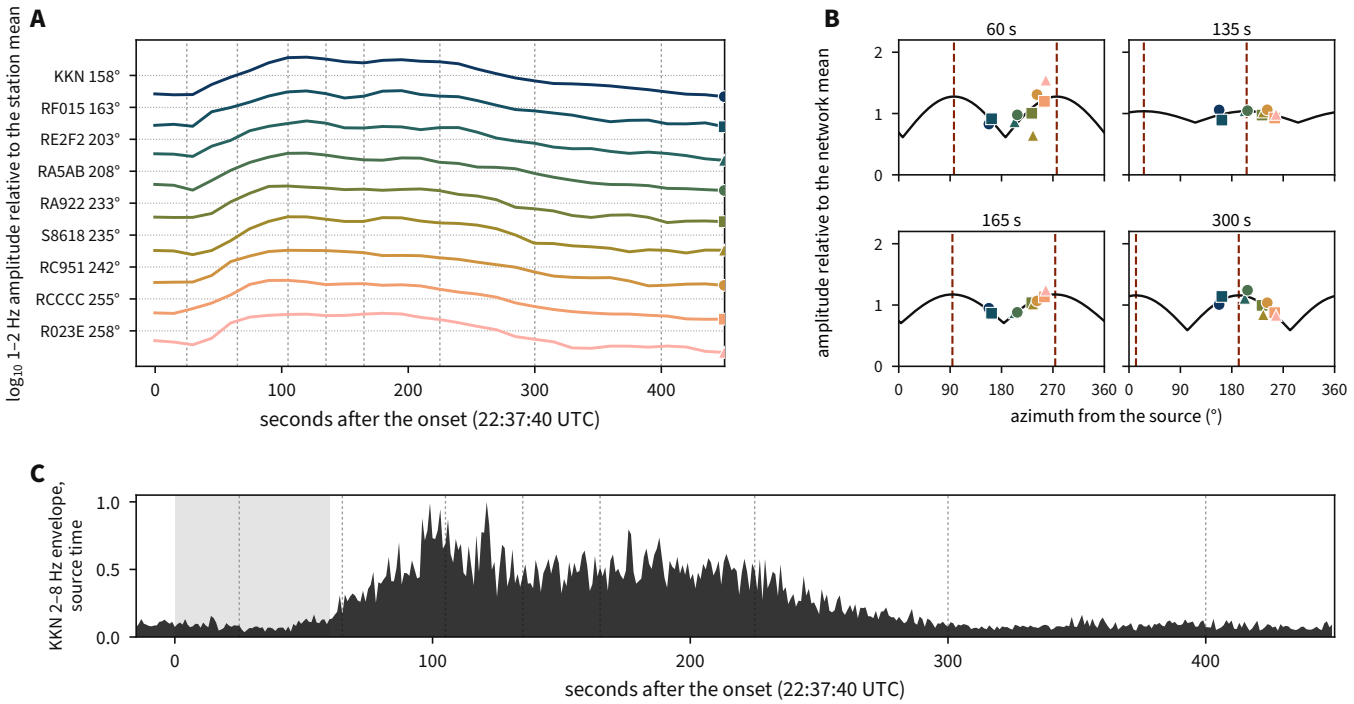



**Figure S4** High-frequency records of the slide at near-field stations. (A) 1–2 Hz vertical RMS amplitude at the nine stations of Fig. 4K in 30-s windows every 15 s, moved to source time with the ak135 S-wave travel time and divided by each station's geometric mean over 30–450 s, stacked by azimuth; dotted lines mark the frame times of Fig. 4A–H. (B) Amplitude relative to the network mean against azimuth in four windows, with the isotropic and two-lobed terms, $A_0 + A_2\,|\cos(\phi - \theta)|$, fitted at the axis $\theta$ of Fig. 4K (dashed). The nine stations span 100° in azimuth (Fig. 1A), so each axis comes from the contrast between the ends of the sector. (C) The KKN 2–8 Hz envelope in source time; the shaded first 60 s hold about 2% of the energy of the four pulses (45–145 s).

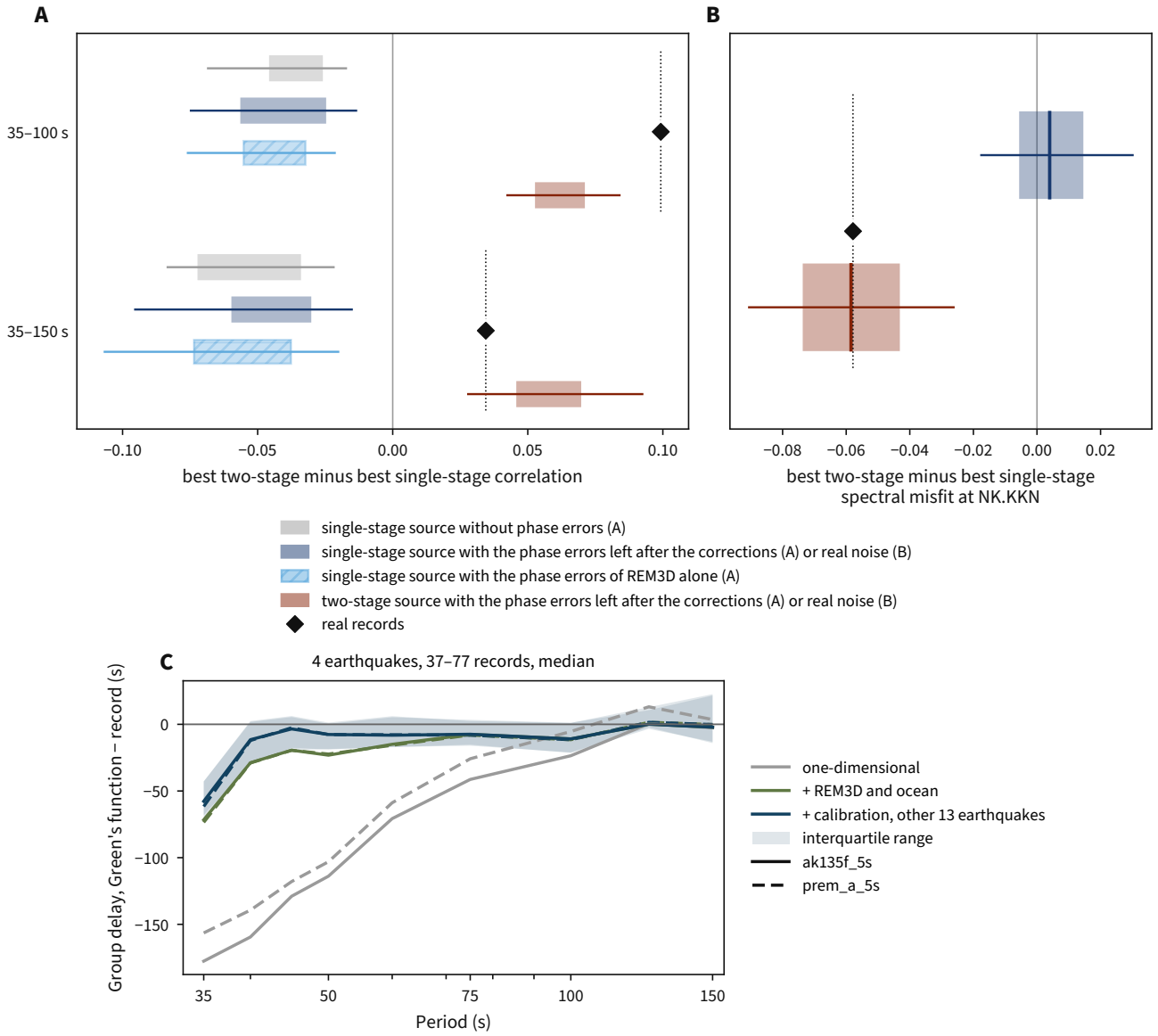



**Figure S5** Phase errors of the Green's functions and the two-stage preference. (A) The difference in correlation with the re-inverted teleseismic force between the best two-stage and the best single-stage simulation (Section S3), at 35–100 s and 35–150 s with ak135f functions. Each box holds this difference for synthetic records of one kind, single-stage simulations without phase errors, single-stage simulations with the errors left after the corrections, single-stage simulations with the errors of REM3D, and the two-stage simulation at +50 s of Table S1 with the errors left after the corrections. The single-stage source is removed from the candidates. Boxes span the quartiles, whiskers the 5–95% range, and the line is the median of 200 records, or 100 with the errors of REM3D. Diamonds are the observed records. (B) The same difference in the spectral misfit at NK.KKN, the best two-stage minus the best single-stage misfit, negative when two stages fit better, for 300 pseudo-records of single-stage simulations, their source again removed, and of the two-stage simulation, with real pre-event noise. The diamond is the record. (C) The phase errors behind these tests, as the group delay of the teleseismic Green's functions on the source-to-station paths, the group arrival minus the distance divided by the group velocity measured on the earthquake record at the same station. The one-dimensional functions, ak135f_5s and prem_a_5s, and their corrected versions (Section S1, each earthquake calibrated from the other 13) are shown as the median over records with a signal-to-noise ratio of at least 5 from four calibration earthquakes 80–266 km from the source, with the interquartile range of the corrected versions. Group arrivals are the envelope maxima of Gaussian narrow-band filters (Bensen et al., 2007). At 40–100 s the corrected functions are 3–12 s early. Below 40 s the corrections rise steeply, and below 35 s, where REM3D has no maps, they are held constant, so at 35 s the corrected functions remain about 60 s early.

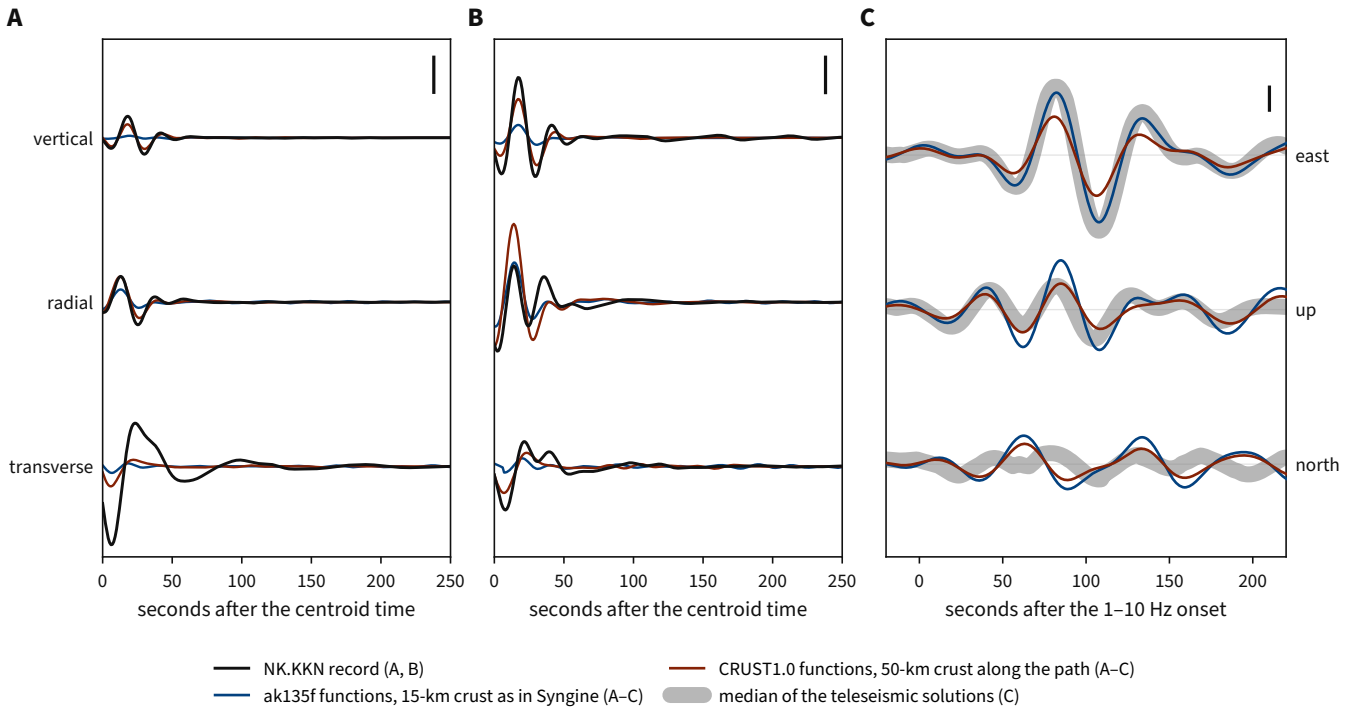



**Figure S6** KKN Green's functions for a Himalayan crust. Single-force functions for NK.KKN computed with pyprop8 (O'Toole and Woodhouse, 2011; Valentine and Sambridge, 2022) in flat layered models reproduce the Syngine ak135f functions of the paper (correlation 0.94–0.99 at 20–80 s for all nine force–component pairs) when the model is ak135f without its ocean, a 15-km crust under 0.3 km of sediment; the crust under the path to KKN is 45–55 km thick (Laske et al., 2013). (A, B) The two Global CMT earthquakes among the 14 calibration earthquakes that KKN recorded, 15 September 2020 and 27 February 2025, about 60 km east-southeast of it, showing the vertical, radial and transverse displacement at 20–80 s, the record against synthetics for the ak135f crust and for the CRUST1.0 crust averaged along the path (50 km over the mantle of ak135f), at the centroid, each synthetic at its best lag (bars 22 and 19 $\mu$m). Over both earthquakes and two locations of each (centroid and USGS epicenter), the thick crust raises the correlation of the vertical from 0.88 to 0.98 and cuts its amplitude error from a factor of 3.1 to 1.7; the continental crust of ak135 does nearly as well (0.97, 1.8); the transverse depends on the location. (C) The KKN force on the Earth from the landslide record, 35–100 s, with the ak135f functions (as in Fig. 2) and with the CRUST1.0 functions, station shift held at zero, against the median of the teleseismic solutions (bar $5 \times 10^{10}$ N). The thick crust fits KKN nearly as well (variance reduction 0.88 against 0.90), halves the force (peak 1.0 against $1.9 \times 10^{11}$ N), keeps its timing and its east component and leaves the remaining differences unchanged; relative to its east force the KKN vertical is 1.7 times the teleseismic ratio (1.8 with ak135f) and its north force remains uncorrelated with theirs. The simulations then imply 2–3 Mm$^3$ for KKN instead of 5–7, so we leave KKN out of the mass range. The spectral test of Fig. S5B favors two stages more strongly with the thick crust (gap $-0.09$ to $-0.10$ against $-0.06$, which no single-stage record reached in 300 trials).

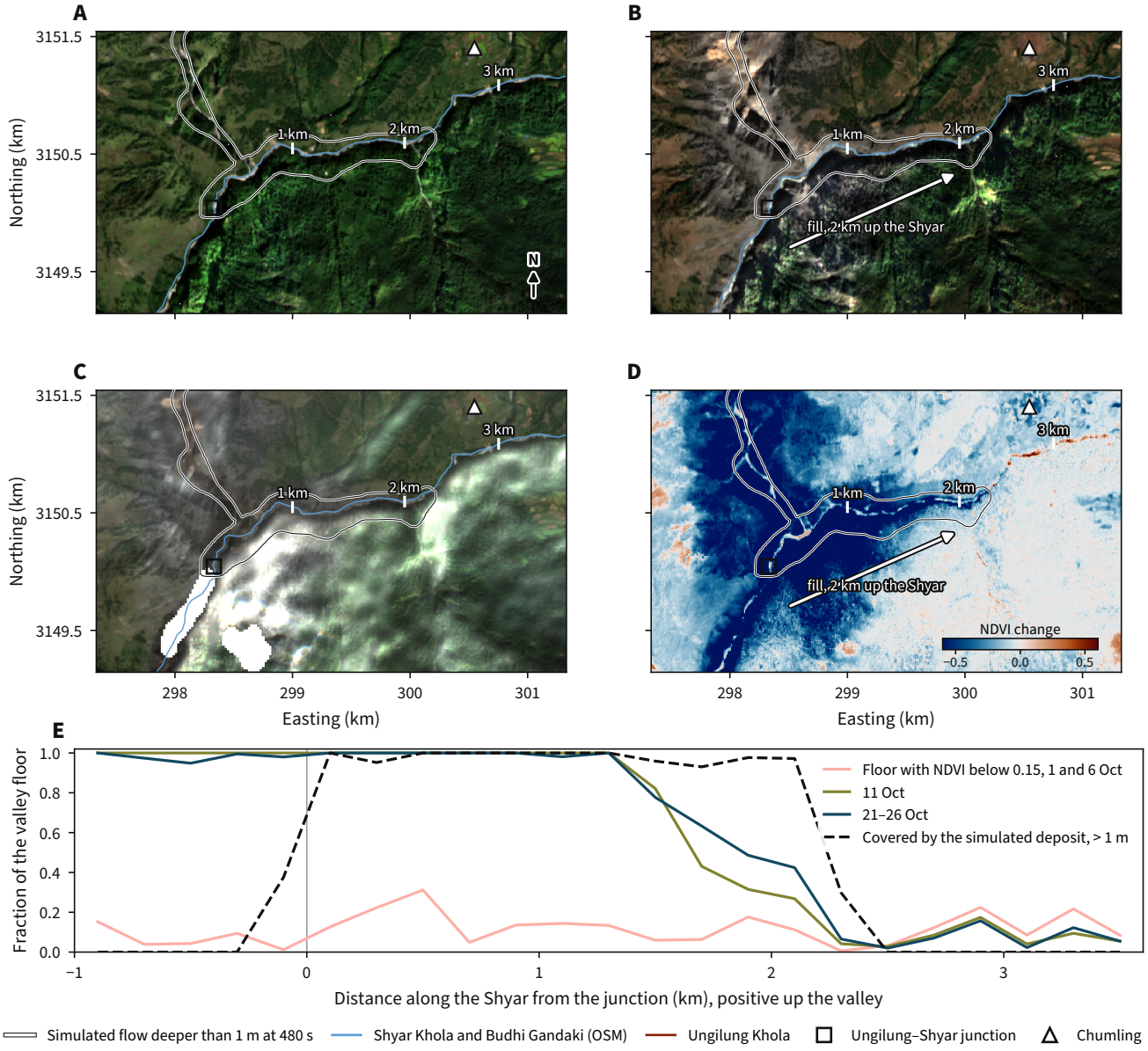



**Figure S7** The deposit at the Ungilung–Shyar junction. (A, B) Sentinel-2 scenes of 1 and 26 October 2026 at 10 m over the junction reach, with the Shyar, the Ungilung, the junction, Chumling, distance marks up the Shyar and the flow of the best simulation (Fig. 4) deeper than 1 m at 480 s. The simulated flow splits at the junction at about 200 s and fills the Shyar 2 km upstream (arrow); on the imagery the valley floor is buried, dark in each band including the shortwave infrared, from the junction to 1.8–2.2 km, and unchanged beyond 2.4 km, where the floor steepens. (C) The scene of 11 October, 05:10 UTC, 6.5 h after the slide, with the fill already at its full extent. (D) Change of NDVI from before the slide (1 and 6 October) to after it (21–26 October); the slopes east of the Ungilung also darkened under the dust of the collapse, so the floor is tested for persistence in E. (E) Fraction of the valley floor within 60 m of the river with NDVI below 0.15 before the slide, on 11 October and on 21–26 October, and the fraction covered by the simulated deposit, in 200-m bins along the Shyar. The floor rises 52 m over the 2 km above the junction, so a pond behind the reported debris dam (National Disaster Risk Reduction and Management Authority (NDRRMA), 2026) would reach the same distance, and the imagery cannot separate debris that ran up the Shyar from mud left by ponded water; either requires a deposit of some tens of meters at the junction.

**Table S2** Common station delays (Section S3). (a) Sensitivity to the common delay scaled by $\alpha$; $\alpha = 1$ is the correction used throughout. KKN cc is the correlation of the KKN force with the corrected teleseismic synthetics of the 35–100 s verticals (ak135f, PREM in parentheses); a parabola through $\alpha = 0.75$, 1 and 1.25 peaks at 0.96 (PREM 0.93). The pulses column gives the number of cases, out of the 32 formed by the four KKN pulses, the four sets and the two Earth models, in which the teleseismic vertical force has the same sign relative to the east–west force as at KKN, downward during the westward pulses and upward during the eastward ones. The VR column is the variance reduction of the 35–100 s vertical inversion. It stays within 0.02 for all $\alpha$ because a common delay reshapes the force without changing the fit. Release times are absolute (seconds after the 1–10 Hz onset), as the range over the four sets with ak135f, for the single-stage reference and the two-stage simulation at +50 s of Table S1, which KKN releases at +47 and $-5$ s for each $\alpha$. The correlation difference is the best two-stage minus the best single-stage correlation among the 19 single-stage and lower-first simulations, as in Fig. S5, on each set with ak135f and as the mean over the four sets with PREM in parentheses. (b) Synthetic trials at 35–100 s as in Section S3 (ak135f, PREM in parentheses), 400 single-stage trials and the two-stage simulation at +50 s kept among the candidates. In the consistent cases the generating and the inverting functions both contain the scaled delay and the threshold is the observed difference at the same $\alpha$; in the mismatched cases only the generating functions contain it, the records are inverted with the functions of the paper and the threshold is the observed difference at $\alpha = 1$. At 35–150 s no single-stage trial reaches the threshold in the consistent case at 0.75 or with the excitation pattern, 1 of 400 does at 1.25, where the difference is 0.007, and 13 of 400 (PREM 6) do with the generating functions at 0.75. At $\alpha = 0.5$ the best release of the single-stage simulation moves by about 52 s to the edge of the release grid, against +47 s at KKN, so those trials are omitted; † denotes the same artifact with PREM.

**(a)**

| | | | | release (s) | | correlation difference | | | | |
|---|---|---|---|---|---|---|---|---|---|---|
| $\alpha$ | KKN cc | pulses | VR | single stage | two-stage | Z 35–100 | Z 35–150 | Love | Z + H | mean |
| 1.25 | 0.56 (0.55) | 31/32 | 0.52 | −10 to +45 | −12 to −8 | +0.03 | +0.01 | −0.06 | 0.00 | +0.01 (+0.03) |
| 1.00 | 0.69 (0.67) | 32/32 | 0.52 | +40 to +45 | −10 to −5 | +0.10 | +0.03 | +0.05 | +0.08 | +0.07 (+0.07) |
| 0.75 | 0.62 (0.64) | 28/32 | 0.53 | +42 to +47 | −8 to −3 | +0.05 | +0.03 | −0.02 | +0.01 | +0.02 (+0.03) |
| 0.50 | 0.39 (0.42) | 25/32 | 0.53 | +42 to +47 | −8 to +46 | −0.01 | −0.05 | −0.06 | −0.04 | −0.04 (−0.02) |
| 0.25 | 0.15 (0.18) | 20/32 | 0.53 | +42 to +98 | +42 to +53 | +0.07 | −0.09 | −0.09 | −0.02 | −0.03 (−0.04) |
| 0.00 | 0.01 (0.03) | 17/32 | 0.53 | +42 to +98 | +42 to +53 | +0.03 | −0.01 | 0.00 | +0.04 | +0.02 (0.00) |

**(b)**

| | | | single stage | | | two-stage simulation, |
|---|---|---|---|---|---|---|
| case | $\alpha$ | threshold | median | maximum | $\geq$ threshold (of 400) | median |
| consistent | 1.25 | 0.03 (0.04) | −0.03 (−0.42†) | +0.002 (−0.209†) | 0 (0) | 0.06 (0.06) |
| consistent | 1.00 | 0.10 (0.10) | −0.03 (−0.03) | +0.003 (+0.004) | 0 (0) | 0.06 (0.06) |
| consistent | 0.75 | 0.05 (0.05) | −0.03 (−0.03) | +0.002 (+0.005) | 0 (0) | 0.06 (0.06) |
| mismatched | 1.25 | 0.10 (0.10) | −0.04 (−0.08) | +0.105 (+0.089) | 1 (0) | 0.03 (0.03) |
| mismatched | 0.75 | 0.10 (0.10) | +0.03 (+0.03) | +0.073 (+0.071) | 0 (0) | 0.11 (0.10) |
| excitation pattern | 1.00 | 0.10 (0.10) | −0.03 (−0.02) | +0.010 (+0.012) | 0 (0) | 0.05 (0.05) |

# References


Bensen, G. D., Ritzwoller, M. H., Barmin, M. P., Levshin, A. L., Lin, F., Moschetti, M. P., Shapiro, N. M., and Yang, Y. Processing seismic ambient noise data to obtain reliable broad-band surface wave dispersion measurements. *Geophysical Journal International*, 169(3):1239–1260, 2007. doi: 10.1111/j.1365-246X.2007.03374.x.

Chao, W.-A., Zhao, L., Chen, S.-C., Wu, Y.-M., Chen, C.-H., and Huang, H.-H. Seismology-based early identification of dam-formation landquake events. *Scientific Reports*, 6(1):19259, 2016. doi: 10.1038/srep19259.

Earth Resources Observation and Science (EROS) Center. Landsat 8-9 Operational Land Imager / Thermal Infrared Sensor Level-1, Collection 2 [Data set]. U.S. Geological Survey, 2020. doi: 10.5066/P975CC9B.

Ekström, G. and Stark, C. P. Simple scaling of catastrophic landslide dynamics. *Science*, 339(6126):1416–1419, 2013. doi: 10.1126/science.1232887.

Laske, G., Masters, G., Ma, Z., and Pasyanos, M. Update on CRUST1.0 – A 1-degree Global Model of Earth's Crust. In *Geophysical Research Abstracts*, volume 15. EGU General Assembly, 2013. Abstract EGU2013-2658.

Masters, G., Woodhouse, J. H., and Gilbert, F. Mineos v1.0.2 [Computer software]. Computational Infrastructure for Geodynamics, https://geodynamics.org/resources/mineos, 2011.

Moulik, P., Lekic, V., Romanowicz, B., Ma, Z., Schaeffer, A., Ho, T., Beucler, E., Debayle, E., Deuss, A., Durand, S., Ekström, G., Lebedev, S., Masters, G., Priestley, K., Ritsema, J., Sigloch, K., Trampert, J., and Dziewonski, A. M. Global reference seismological data sets: multimode surface wave dispersion. *Geophysical Journal International*, 228(3):1808–1849, 2021. doi: 10.1093/gji/ggab418.

National Disaster Risk Reduction and Management Authority (NDRRMA). An avalanche and massive landslide triggered the devastating Budhi Gandaki flood, report finds. Technical report as reported by OnlineKhabar, 13 October 2026, https://english.onlinekhabar.com/avalanche-landslide-budhi-gandaki-flood.html, 2026.

O'Toole, T. B. and Woodhouse, J. H. Numerically stable computation of complete synthetic seismograms including the static displacement in plane layered media. *Geophysical Journal International*, 187(3):1516–1536, 2011. doi: 10.1111/j.1365-246X.2011.05210.x.

Shugar, D. H. PlanetScope comparison of the Budhi Gandaki flood source, 1 and 14 October 2026. Bluesky post, https://bsky.app/profile/watershedlab.bsky.social/post/3mxtkwxdaok2u, 14 October 2026; imagery © 2026 Planet Labs PBC, 2026.

Valentine, A. P. and Sambridge, M. pyprop8: A lightweight code to simulate seismic observables in a layered half-space. *Journal of Open Source Software*, 7(76):4217, 2022. doi: 10.21105/joss.04217.

Wang, Z. and Dahlen, F. A. Spherical-spline parameterization of three-dimensional Earth models. *Geophysical Research Letters*, 22(22):3099–3102, 1995. doi: 10.1029/95GL03080.